Supplementary Information

Brittle materials-based fully stretchable organic light-emitting diodes

Chuang Xue[1,2], Xiaoli Zhao[1,], Ning He[1], Yanping Ni[1], Lequn Yuan[1], Junru Zhang[1], Pengbo Xi[1], Baoying Sun[1], Mingxin Zhang[1], Yanhong Tong[1], Qingxin Tang[1,]* and Yichun Liu[1]*

[1] State Key Laboratory of Integrated Optoelectronics and Key Laboratory of UV-Emitting Materials and Technology of Ministry of Education, College of Physics, Northeast Normal University, Changchun 130024, PR China.

[2] Jilin Provincial Key Laboratory of Wide Bandgap Semiconductor Material Growth and Device Applications, College of Information Technology, Jilin Normal University, Changchun 130103, PR China.

E-mail: tangqx@nenu.edu.cn; zhaoxl326@nenu.edu.cn

Table of Contents

Supplementary Fig. S33 | Comparison of electrical conductivity, optoelectronic performance, and mechanical stability between PEDOT:PSS and PEDOT:PSS/SWCNTs electrodes and corresponding devices.

Supplementary Fig. S34 | Energy-level alignment diagram of fully stretchable SMOS-OLEDs with different colors and the molecular structures of the corresponding emissive materials.

Supplementary Fig. S35 | Normalized luminance variation of the three devices during repeated uniaxial stretch–release cycles at 30% strain.

Supplementary Tables

Supplementary Table S1 | Comparison of this study with recently reported stretchable LEDs, including organic, polymer, QD, and perovskite LEDs.

Supplementary Table S2 | Surface energies and their polar and dispersive components of deionized (DI) water and diiodomethane (DIM).

Supplementary Table S3 | Contact angles of DI water and DIM on Si and OTS/Si surfaces and the corresponding polar and dispersive components of surface energy.

Supplementary Note S1 | Comprehensive comparison of peeling-assisted and conventional layer-by-layer deposition strategies for PEDOT:PSS/SWCNTs electrodes.

Compared with the PEDOT:PSS/SWCNTs electrode prepared by the conventional layer-by-layer (LBL) deposition process, the peeling-assisted approach significantly reduces the surface roughness of the electrode (Supplementary Fig. S7). Specifically, the root-mean-square (RMS) roughness of the LBL-deposited stacked electrode is as high as 3.94 nm, whereas that of the peeled electrode is only 0.79 nm. This pronounced difference primarily arises from the fact that the upper layer of the stacked electrode is a SWCNTs film. Owing to their high aspect ratio, SWCNTs are prone to mutual overlap during the spray-coating process, resulting in an uneven surface morphology. Furthermore, the weak van der Waals forces between SWCNTs drive them to attract each other and form aggregates, leading to an increased surface roughness. Such a rough surface could severely hinder the subsequent continuous and uniform deposition of the ultrathin SMOS layers, and easily induce localized electric field concentration, thereby increasing the risk of leakage current or localized short circuits. In contrast, the SWCNTs in the peeled electrode are embedded into the IBL, and the electrode surface after peeling corresponds to the pristine interface between PEDOT:PSS and octadecyltrichlorosilane-modified silicon (OTS/Si). Consequently, the RMS roughness of the peeled embedded electrode is substantially lower than that of the stacked counterpart.

To obtain such a low-roughness embedded electrode, the OTS/Si substrate is critical to the peeling-assisted process. Specifically, the Si substrate was first treated with O_2 plasma to hydroxylate the surface and was then immersed in an OTS/heptane solution (1:1000) to form a low-adhesion, hydrophobic surface. The OTS/Si substrate plays two important roles. First, it serves as a rigid and flat fabrication platform, which is beneficial for spin coating, spray coating, photolithographic patterning, and O_2 plasma etching of the PEDOT:PSS/SWCNTs anode, thereby enabling well-defined patterned electrodes with uniform morphology. In contrast, if the electrode is directly deposited and patterned on polymeric substrates such as the IBL or ADL, the substrate may undergo deformation or swelling during solvent treatment, UV exposure, development, or plasma etching, resulting in electrode pattern distortion. Second, the Cl groups in OTS molecules can interact with hydroxyl groups on the Si substrate, spontaneously forming an ordered molecular assembly layer at the interface (Supplementary Fig. S8). The resulting OTS/Si substrate exhibits a hydrophobic and weakly polar surface, which significantly reduces the adhesion between the substrate surface and the overlying embedded electrode. Consequently, after the patterned PEDOT:PSS/SWCNTs anode is embedded into the IBL and supported by PDMS, it can be nondestructively peeled off from the rigid Si carrier.

To verify the hydrophobicity of the Si substrate after OTS modification, we first investigated the change in surface properties before and after modification by contact-angle measurements. As shown in Supplementary Fig. S9a, after OTS modification, the water contact angle of the Si substrate increased from 36.1° to 102.8°, indicating the formation of a hydrophobic surface. In addition, the modified OTS/Si substrate exhibited a smooth surface morphology, with an RMS roughness of only 0.64 nm (Supplementary Fig. S9c). Furthermore, we calculated the surface energies of the Si and OTS/Si substrates. Contact angles of two solvents with known surface energy polar and dispersive components on the surface of the films are first required, and then substituted into the Owens-Wendt-Rabel-Kaelble and Young equations (Equation 1) to calculate the polar and dispersive components of the surface energy[1]. The sum of these two components is the total surface energy of the material. In Equation 1, γ^{p} and γ^{d} are the polar and dispersive components of the surface energy of the unknown material, and $\gamma_{lv}{}^{p}$ and $\gamma_{lv}{}^{d}$ are the polar and dispersive components of the surface energy of the known solvent, respectively. The two most commonly used test solvents in this experiment are deionized water (DI water) as the polar solvent and diiodomethane (DIM) as the non-polar solvent. The polar component, dispersive component and surface energy of DI water is 51.0 mJ/m^2, 21.8 mJ/m^2 and 72.8 mJ/m^2, respectively (Supplementary Table S2). The polar component, dispersion component and surface energy of DIM is 0.0 mJ/m^2, 50.8 mJ/m^2 and 50.8 mJ/m^2, respectively. The polar component, dispersive component and total surface energy of Si are calculated from Equation 1 as 26.40 mJ/m^2, 38.89 mJ/m^2 and 65.29 mJ/m^2, respectively. The polar component, dispersive component and total surface energy of OTS-Si are calculated from Equation 1 as 1.77 mJ/m^2, 16.22 mJ/m^2 and 17.99 mJ/m^2, respectively (Supplementary Fig. S9b and Table S3). These results demonstrate that OTS modification significantly reduces the surface energy of the Si substrate from 65.29 to 17.99 mJ/m^2. This decrease effectively weakens the adhesion between the embedded electrode and the OTS/Si substrate, thereby enabling nondestructive peeling. The three-dimensional (3D) optical microscopy images in Supplementary Fig. S10a further confirm that the electrode remains intact before and after peeling from the OTS/Si substrate. After peeling, the sheet resistance of the electrode only slightly increases from 90 to 92 Ω/sq, corresponding to an increase of only 2.2%, indicating that the peeling process has a negligible effect on the electrical conductivity of the electrode (Supplementary Fig. S10b). Moreover, the peeled 25 nm-thick SWCNTs-based composite electrode simultaneously delivers a high optical transmittance of 85.8%, a high electrical conductivity of 2717 S/cm, and excellent stretching stability, further confirming its suitability as an ultrathin transparent stretchable anode (Supplementary Figs. S11, 12). Notably,

the peeled device achieves maximum CE and EQE values of 85.7 cd/A and 24.7%, respectively, outperforming both rigid OLEDs based on the same material system fabricated by conventional layer-by-layer deposition and ITO-based rigid OLEDs (Supplementary Fig. S13).

$$1 + \cos\theta = \frac{2(\gamma^{p})^{1/2}(\gamma_{1v}^{p})^{1/2}}{\gamma_{1v}} + \frac{2(\gamma^{d})^{1/2}(\gamma_{1v}^{d})^{1/2}}{\gamma_{1v}} \quad \text{Equation 1}$$

Above all, compared with the conventional layer-by-layer deposition method, the peeling-assisted anode fabrication process on the OTS/Si substrate offers three major advantages. First, the rigid OTS/Si substrate facilitates high-quality patterning. Second, the hydrophobic OTS interface enables nondestructive peeling of the patterned anode. Third, this process yields an embedded electrode with extremely low surface roughness, providing a favorable interfacial foundation for the subsequent deposition of the upper SMOS layers and cathode.

Supplementary Note S2 | Biaxial stretching characterization of crack-guided stretchable OLEDs.

In practical applications, stretchable OLEDs are inevitably subjected to multidirectional and spatially non-uniform deformations. Therefore, we investigated the stress concentration, crack evolution, and EL performance of the crack-guided stretchable OLEDs under biaxial stretching (0%, 30%, 50%, and 80% strain). Specifically, 3D optical microscopy images obtained under biaxial stretching at 30%, 50%, and 80% strain illustrate that the PEDOT:PSS/SWCNTs top electrode maintains a continuous surface morphology at both low and high magnifications, without obvious microcrack propagation or surface damage (Supplementary Fig. S16). These observations indicate that the applied biaxial strain is not released through uncontrolled surface cracking. To directly visualize the internal crack distribution at the nanoscale, cross-sectional FIB-SEM characterization was carried out under the same biaxial strains (Supplementary Fig. S17). In the unstretched state, the device layers are continuous and uniform, without obvious cracks or interfacial defects. At 30% biaxial strain, tiny localized nanocracks, such as a 42 nm-wide gap, begin to initiate in the brittle active layer region due to local stress concentration. As the biaxial strain increases to 50% and 80%, the number of nanocracks increases moderately. Importantly, these cracks remain confined within the active layer and do not propagate through the entire device stack. Meanwhile, no obvious interfacial delamination or layer slippage is observed among the anode, active layer, cathode, and IBLs. These results indicate that even under biaxial deformation, the cracks are still effectively guided into localized nanoscale strain-dissipation units rather than developing into destructive through-layer fractures.

To further clarify the spatial stress distribution under biaxial deformation, finite element simulations were performed using COMSOL Multiphysics (Supplementary Fig. S18). The results reveal that the stress within the central functional region remains relatively uniform under biaxial stretching. As the biaxial strain increases from 30% to 50% and 80%, the maximum stress rises from 21.8 to 36.3 and 58.0 MPa, respectively, accompanied by a progressive expansion of the high-stress regions around the device perimeter. Despite the increasing stress level, no severe localized stress concentration is observed in the central active region, indicating that the hierarchical stress-regulation architecture effectively redistributes the applied biaxial load toward the surrounding boundary regions. This stress-distribution behavior helps suppress uncontrolled crack initiation and catastrophic crack propagation within the functional device area. The EL performance further supports this mechanism. Under biaxial stretching, the device retains 95.9%, 86.4%, and 70.2% of its initial luminance at 30%, 50%,

and 80% strain, respectively (Supplementary Fig. S19). These results demonstrate that although the number of localized nanocracks slightly increases with strain, they remain within a structurally and electrically tolerable regime and do not severely disrupt the vertical charge injection–transport–recombination pathway.

Supplementary Note S3 | Cyclic deformation characterizations of crack-guided stretchable OLEDs.

We performed morphological characterization of crack evolution and EL performance measurements on devices subjected to repeated stretch–release cycles to verify the robustness of our crack-guiding strategy against cyclic mechanical deformation. As shown in Supplementary Fig. S23, we first examined the surface morphology of the device in the pristine state and after 500, 1,000, and 1,500 uniaxial stretch–release cycles at 30% strain using 3D optical microscopy. During the entire cycling process, both the low-magnification images (Supplementary Fig. S23a) and high-magnification images (Supplementary Fig. S23b) mainly show the surface morphology of the PEDOT:PSS/SWCNTs top electrode, without obvious surface microcracks, macroscopic crack propagation, or surface damage. This result indicates that repeated stretching does not induce catastrophic surface fracture or uncontrolled crack accumulation. In other words, the cyclic deformation of the device is not accommodated by random surface cracking, but is effectively confined and regulated within the designed multilayer architecture.

To further reveal the internal crack evolution during cyclic stretching, we performed FIB-SEM characterization after different numbers of uniaxial stretch–release cycles. As revealed in Supplementary Fig. S24, after 500, 1,000, and 1,500 cycles at 30% strain, only a limited number of localized nanocracks are observed inside the device, and these cracks remain confined within the active layer without evolving into microcracks penetrating through the entire functional stack. Notably, as the cycle number increases from 500 to 1,500, the number of nanocracks shows only a slight increase, indicating that a small amount of local residual stress accumulated during repeated stretching is gradually released through the formation of additional confined nanocracks. With further cycling, the crack morphology tends to reach a relatively stable state, without rapid crack multiplication, obvious crack widening, or uncontrolled lateral propagation. Meanwhile, no obvious interfacial delamination or lateral dislocation is observed among the anode (PEDOT:PSS/SWCNTs), active layer, cathode (Al), and interfacial buffer layers (IBL, NOA68). These findings verified that the cracks generated during repeated stretching are not randomly accumulated destructive defects, but nanoscale strain-dissipation units guided and confined by the hierarchical stress-regulation architecture. If the cracks propagated uncontrollably during cycling, they would further evolve into through-layer microcracks or interfacial delamination, thereby disrupting the vertical charge injection–transport–recombination pathway and causing rapid device failure. In contrast, the FIB-SEM results show that the nanocracks after cyclic stretching remain localized and confined, demonstrating that

our crack-guiding strategy effectively suppresses catastrophic crack propagation and preserves the structural integrity of the multilayer device during repeated deformation.

The electrical performance further supports this morphological mechanism. As depicted in Fig. 4i, the green-emitting device retains 86.5% of its initial luminance even after 1,500 uniaxial stretching-releasing cycles under 30% strain. This result indicates that the sub-wavelength-scale nanocracks formed after cycling do not significantly compromise the EL performance of the device. This can be mainly explained by two factors. First, the visible emission wavelength of the OLED (400-700 nm) is one order of magnitude larger than the crack width, precluding the formation of detectable optical scattering-induced dark stripes via classical diffraction effects. Second, the device's vertical charge injection-transport-recombination paradigm remains intact, as the cracks merely partition the active layer rather than disrupting the global vertical charge pathway. In this context, this is analogous to partitioning the OLED into micron-scale subunits separated by nanocracks, each retaining efficient carrier injection, transport, and exciton recombination, thereby ensuring stable emission after cyclic stretching. Furthermore, the blue, yellow, and red devices retain 82.9%, 83.7%, and 80.5% of their initial luminance after 1,500 cycles, respectively (Supplementary Fig. S35). The excellent cycling stability of the multicolor devices can be attributed to the hierarchical stress-regulation architecture, in which the IBLs and ADL effectively dissipate mechanical stress and suppress catastrophic crack propagation during repeated stretching. Such consistent cyclic stability across multicolor devices demonstrates that our nanocrack-guiding strategy is not limited to a specific emissive material system, but can be broadly extended to diverse SMOS-based OLED architectures.

Moreover, to better emulate multidirectional deformation encountered in practical skin-mounted scenarios, we further performed biaxial cyclic stretching tests at 20% strain. As displayed in Supplementary Fig. S25, during the entire biaxial cycling process, both the low- and high-magnification 3D optical microscopy images show a relatively smooth and continuous surface morphology of the PEDOT:PSS/SWCNTs top electrode, without obvious surface microcracks, macroscopic crack propagation, or surface damage. This result suggests that even under multidirectional cyclic deformation, repeated biaxial stretching does not induce obvious surface fracture or uncontrolled crack accumulation. The internal crack evolution under biaxial cycling was further investigated by cross-sectional FIB-SEM. As shown in Supplementary Fig. S26, after 500, 1,000, and 1,500 biaxial stretch–release cycles at 20% strain, only a few localized nanocracks are observed within the active layer, which remain confined without propagating through the whole device stack, similar to the crack evolution observed under

uniaxial cyclic stretching. Meanwhile, no obvious interfacial delamination or layer slippage is observed among the anode, active layer, cathode, and IBLs. Although the number of confined nanocracks slightly increases with cycling, they do not evolve into through-layer microcracks or laterally propagated cracks, further indicating that the hierarchical stress-regulation architecture remains effective under biaxial deformation. Consistent with these morphological features, the green-emitting device preserves 81.2% of its initial luminance after 1,500 biaxial stretch–release cycles at 20% strain (Supplementary Fig. S22). This retained luminance confirms that the confined nanocracks generated during biaxial cycling remain within a structurally and electrically tolerable regime, without causing severe disruption to the vertical charge injection–transport–recombination pathway.

The above results, both from surface/internal crack morphology/distribution characterization and cyclic EL performance, collectively demonstrate that the guided nanocracks remain confined within the active layer and well regulated during repeated stretching, further substantiating the reliability of our crack-guiding strategy for high-performance stretchable OLEDs.

Supplementary Note S4 | Comparison of stress distribution and crack evolution in ITO/active layer/Al and PEDOT:PSS/SWCNTs/active layer/Al architectures.

To further clarify the practical significance of our electrode design, this section presents a direct comparison between the conventional ITO/active layer/Al architecture and the PEDOT:PSS/SWCNTs/active layer/Al architecture developed in this work. Although ITO is a mature transparent anode material in conventional OLED technology, it possesses several inherent limitations when applied to fully stretchable OLEDs. First, as an indium-based oxide, the scarcity and high cost of indium present substantial challenges for large-area and scalable optoelectronic manufacturing. Second, the fabrication of high-quality ITO electrodes typically relies on sputtering processes, often requiring high-temperature post-treatments (above 200 °C) to optimize conductivity and transparency. Such processing conditions are incompatible with soft elastomeric substrates or multilayer stretchable device stacks, as they can induce thermal damage to underlying functional layers or compromise interfacial integrity. Furthermore, ITO is intrinsically brittle, with a high Young's modulus of 120 GPa and a low elongation at break of only approximately 1%. Consequently, its intrinsic material properties render it incapable of tolerating large tensile deformations. These limitations are also the main reason why extensive research efforts have been devoted to developing various flexible and stretchable electrodes as alternatives to conventional ITO electrodes.

Notably, the limitation of the conventional ITO/Al architecture does not simply arise from the brittleness of ITO itself. In fact, the SMOS-based active layer in our device is even more brittle, with an elongation at break of approximately 0.5%. Therefore, the bottleneck is not merely whether a constituent material is brittle, but rather how the stress distribution and crack evolution across the multilayer device architecture are regulated. In the conventional ITO/active layer/Al architecture, both ITO (≈120 GPa, ≈1% elongation at break) and Al (≈67.5 GPa, ≈5% elongation at break) serve as rigid electrodes. Such mechanical incompatibility first manifests as preferential fracture of the top ITO electrode. Owing to its high modulus and low elongation at break, ITO cannot accommodate tensile deformation or dissipate stress through elastic or plastic deformation under applied strain, and therefore readily develops dense, oriented cracks at relatively low tensile strain.

As shown in Supplementary Fig. S29a, 3D optical microscopy images clearly reveal that, when the ITO/active layer/Al architecture is stretched to 80% strain, dense, continuous, and large-scale cracks appear on the device surface, indicating pronounced brittle fracture of the top ITO electrode. More importantly, these cracks are not confined to the isolated ITO layer; instead, they fundamentally alter the local stress fields throughout the entire multilayer stack. Because

the low-modulus active layer is sandwiched between the top ITO and bottom Al rigid electrodes, this dual-rigid-electrode configuration lacks a rational modulus gradient, making it incapable of effectively dissipating tensile stress. Consequently, the premature fracture of the top ITO layer is expected to induce severe localized stress concentration at the crack tips, driving the cracks to propagate downward through the underlying functional layers.

Cross-sectional FIB-SEM characterization further validates this stress-transfer mechanism and visually captures the resulting structural failure. Under 80% tensile strain, pronounced penetrating cracks can be observed in the ITO/active layer/Al architecture (Supplementary Fig. S29b). These cracks initiate near the upper ITO electrode due to a high modulus and low elongation at break, and subsequently propagate downward along the thickness direction, penetrating through the active layer and further extending into the Al cathode region. Notably, interfacial delamination at the ITO/NOA68 interface can also be observed around the cracks, indicating that the brittle ITO layer not only fractures during stretching but also weakens the adhesion stability of adjacent interfaces through crack-tip-induced local stress concentration. Such penetrating cracks and interfacial delamination directly disrupt the vertical charge injection, transport, and recombination pathways, ultimately leading to severe performance degradation or even device failure.

Therefore, our strategy is not aimed at realizing the nearly impossible goal of rendering rigid and brittle ITO intrinsically stretchable. Instead, we reconstruct the mechanical boundary conditions of the OLED functional stack by introducing an asymmetric electrode architecture, thereby establishing a rational modulus gradient and a compatible elongation-at-break distribution. In sharp contrast, the asymmetric gradient modulus architecture (low-modulus PEDOT:PSS/SWCNTs top electrode and high-modulus Al bottom electrode) developed in this work effectively mitigates the failure modes associated with the aforementioned dual-rigid-electrode architecture. The synergistic regulation of Young's modulus and elongation at break in this asymmetric design is critical for crack control: the PEDOT:PSS/SWCNTs top electrode (≈4.4 GPa, ≈10% elongation at break) accommodates partial tensile deformation to reduce interfacial stress, while the Al bottom electrode (≈67.5 GPa, ≈5% elongation at break) provides mechanical constraint to guide crack propagation (Supplementary Fig. S29c, d). In this configuration, the mechanical gradient introduced by the asymmetric electrodes dictates nanocrack formation, with interfacial stress efficiently dissipated through the Al/active layer interface. Furthermore, leveraging the stress-sensitive nature of SMOS and the directional stress guidance from the asymmetric elongation at break distribution, nanocracks preferentially propagate along the vertical direction rather than the lateral direction, avoiding the formation

of horizontal dislocations that would sever charge transport pathways. Therefore, compared with the conventional ITO/active layer/Al architecture, the advantage of the PEDOT:PSS/SWCNTs/active layer/Al gradient modulus architecture developed in this work is not limited to overcoming the issues associated with ITO, including indium scarcity and sputtering/high-temperature processing. Remarkably, as shown in Supplementary Fig. S13, the optoelectronic performance of the device based on the PEDOT:PSS/SWCNTs composite electrode (maximum CE of 85.7 cd/A and EQE of 24.7%) even surpasses that of the conventional ITO-based reference device (maximum CE of 65.5 cd/A and EQE of 18.9%). This improvement can be attributed to the improved surface morphology and more favorable work-function matching of the embedded PEDOT:PSS/SWCNTs electrode.

In summary, the failure of the conventional ITO/Al architecture primarily originates from the irrational modulus gradient and incompatible elongation-at-break distribution under dual-rigid-electrode confinement. By contrast, the asymmetric PEDOT:PSS/SWCNTs/Al electrode architecture developed in this work effectively modulates stress concentration and crack propagation, confining cracks to localized nanocracks within the active layer while preventing penetrating cracks, interfacial delamination, and device failure. These results further validate the necessity and effectiveness of our crack-guiding strategy for constructing high-efficiency, fully stretchable SMOS-based OLEDs.

Supplementary Note S5 | Design window of the electrode modulus-gradient architecture.

To clarify the acceptable design window of the electrode modulus gradient and further define the mechanistic boundaries of the active crack engineering strategy, we systematically expanded our experimental matrix. Specifically, a decoupling analysis of this asymmetric system was performed using a single-variable controlled approach (i.e., fixing one electrode while varying the counter electrode). On the one hand, with the original Al cathode fixed, PEDOT:PSS and SWCNTs were separately used as the anode to evaluate the influence of low-modulus polymer and nanonetwork anodes on crack regulation. On the other hand, with the original PEDOT:PSS/SWCNTs composite anode fixed, gold (Au) and silver (Ag) were introduced as alternative cathodes to assess the role of high-modulus metal cathodes in crack regulation.

First, the intrinsic Young's moduli of the respective electrode materials were measured by AFM in mechanical mode. As illustrated in Supplementary Fig. S30, the Young's moduli of PEDOT:PSS and the SWCNTs network (derived from an aqueous SWCNTs dispersion of 0.15 mg/mL) were measured to be approximately 1.5 GPa and 6.8 GPa, respectively, whereas Au and Ag exhibited significantly higher Young's moduli of approximately 77.2 GPa and 81.9 GPa, respectively. Herein, PEDOT:PSS represents a low-modulus polymer thin-film electrode, SWCNTs represent a relatively higher-modulus conductive nanonetwork electrode, and Au and Ag represent high-modulus metal electrodes. Crucially, given that Au and Ag are universally standard materials for high-conductivity transparent or semi-transparent electrodes in state-of-the-art transparent or top-emitting OLEDs, implementing them as comparative cathodes provides profound physical significance. These controls not only allow us to verify whether the modulus-gradient strategy depends specifically on the Al cathode, but also demonstrate that the design principle of using a high-modulus metal electrode as a rigid constraint layer has a certain degree of generality rather than being a material-specific case.

As shown in Supplementary Fig. S31, regardless of whether a low-modulus polymer thin-film anode (PEDOT:PSS, ≈1.5 GPa), a relatively higher-modulus nanonetwork anode (SWCNTs, ≈6.8 GPa), or high-modulus metal cathodes (Au, ≈77.2 GPa; Ag, ≈81.9 GPa) were implemented, both low- and high-magnification 3D optical microscopy images mainly show the surface morphology of the top anode, without obvious surface microcracks, macroscopic crack propagation, or severe structural damage. This result indicates that, within this asymmetric system, the devices do not undergo catastrophic surface fracture or uncontrolled crack accumulation under 80% tensile strain. To further reveal the internal crack evolution of devices with different electrode moduli during stretching, we performed cross-sectional FIB-

SEM characterization. As revealed in Supplementary Fig. S32, under 80% tensile strain, the internal cracks remain at the nanoscale and are confined within the active layer, without penetrating through the entire functional stack or developing into large-scale microcracks. Meanwhile, no obvious interfacial delamination or lateral dislocation is observed among the anode, active layer, cathode, and interfacial buffer layers. This behavior is consistent with that observed in the original PEDOT:PSS/SWCNTs (≈4.4 GPa)/active layer/Al (≈67.5 GPa) architecture.

Consequently, these results demonstrate that the proposed modulus gradient architecture possesses a robust acceptable design window, rather than relying on one specific combination of modulus values. In other words, although the PEDOT:PSS/SWCNTs/active layer/Al architecture represents the optimized structure, the core design principle shows a certain degree of generality. Specifically, the anode side should possess a relatively low-to-intermediate modulus lower than that of the active layer (1.5 GPa $\leq E_{\text{anode}} \leq$ 6.8 GPa, $E_{\text{active layer}} \approx$ 12.5 GPa), enabling it to partially accommodate tensile deformation and reduce interfacial stress. In contrast, the cathode side should possess a high modulus greater than that of the active layer (67.5 GPa $\leq E_{\text{cathode}} \leq$ 81.9 GPa, $E_{\text{active layer}} \approx$ 12.5 GPa), thereby providing mechanical constraint and guiding crack propagation. In this configuration, the mechanical gradient introduced by the asymmetric electrodes dictates nanocrack formation, with interfacial stress efficiently dissipated through the metal cathode/active layer interface. Furthermore, leveraging the stress-sensitive nature of SMOS and the directional stress guidance from the asymmetric elongation at break distribution, nanocracks preferentially propagate along the vertical direction rather than the lateral direction, avoiding the formation of horizontal dislocations that would sever charge transport pathways.

Notably, although the devices utilizing single-component PEDOT:PSS or SWCNTs anodes can reproduce the expected nanocrack-guiding behavior to some extent, this does not imply that they are fully equivalent to the PEDOT:PSS/SWCNTs composite anode in terms of comprehensive device performance. The introduction of SWCNTs (≈6.8 GPa) increases the effective modulus of the composite electrode (≈4.4 GPa) and improves its stretchable stability, whereas PEDOT:PSS (≈1.5 GPa) mainly provides a continuous, smooth, and flat surface. As presented in Supplementary Fig. S33, compared with the single-component PEDOT:PSS electrode, the incorporation of SWCNTs reduces the initial resistance of the electrode from 275 to 92 Ω, indicating that the SWCNTs network significantly enhances the electrode conductivity. Meanwhile, the normalized resistance variation of the PEDOT:PSS/SWCNTs electrode during stretching is slightly lower than that of the pure PEDOT:PSS electrode, with R/R_0 decreasing

from approximately 3.9 to 3.3, which indicates that the introduction of SWCNTs contributes to mitigating resistance degradation under strain. Benefiting from the enhanced anode conductivity and mechanical stability, the PEDOT:PSS/SWCNTs-based device exhibits markedly improved EL performance, with the maximum luminance increasing from 10,715 cd/m^2 for the PEDOT:PSS-based device to 16,050 cd/m^2. Additionally, under a severe tensile strain of 250%, the luminance retention ratio increases from 60.2% to 63.4%.

However, neither utilizing a single-component SWCNTs electrode nor adopting a conventional layer-by-layer stacked SWCNTs/PEDOT:PSS architecture stands as the optimal paradigm, which is fundamentally constrained by the electrode surface topography. As presented in Supplementary Fig. S7a, when the SWCNTs are located on the top surface, the RMS roughness reaches as high as 3.94 nm. Such a configuration inevitably introduces a relatively rough electrode/organic interface due to the overlapped and aggregated SWCNTs network, which can induce local electric-field concentration, non-uniform charge injection, and interfacial defects during the deposition of SMOS active layer. To address this issue, we employed a dry-peeling strategy based on a low-adhesion OTS-Si interface to fabricate the embedded PEDOT:PSS/SWCNTs composite anode. Specifically, the Si substrate was first modified with an OTS monolayer. The Cl groups in OTS molecules can interact with hydroxyl groups on the Si substrate, spontaneously forming an ordered molecular assembly layer at the interface (Supplementary Fig. S8). The resulting OTS/Si substrate exhibits a hydrophobic and smooth surface (Supplementary Fig. S9), which significantly reduces the adhesion between the substrate surface and the overlying embedded electrode. Then, the PEDOT:PSS/SWCNTs electrode is embedded and peeled from the ultra-smooth OTS/Si interface. After peeling, the exposed electrode surface is dominated by the smooth PEDOT:PSS side, while the SWCNTs network is partially embedded underneath. As a result, the roughness of the peeled electrode is reduced to only 0.79 nm (Supplementary Fig. S7d). This structure substantially improves the electrode/organic interface quality, which is beneficial for more efficient hole injection and balanced charge recombination. Therefore, considering surface morphology, electrical conductivity, optoelectronic performance, and mechanical stability, we ultimately selected the dry-peeling fabricated PEDOT:PSS/SWCNTs composite anode as the optimized anode structure.

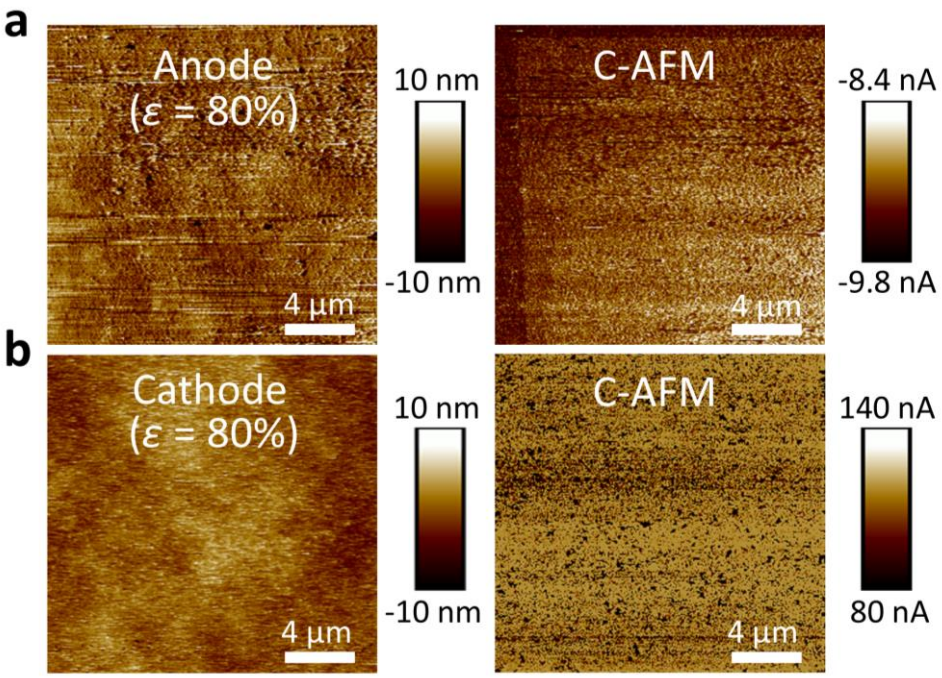

Supplementary Fig. S1 | AFM and conductive AFM (C-AFM) images under 80% tensile strain. a Anode (PEDOT:PSS/SWCNTs). **b** Cathode (Al).

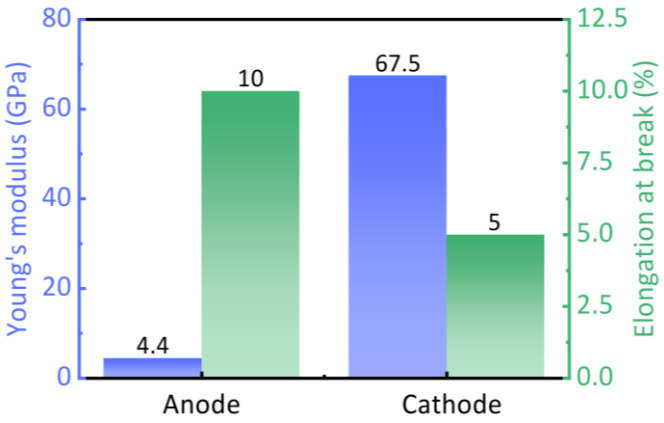

Supplementary Fig. S2 | Young's modulus and elongation at break of the anode and cathode.

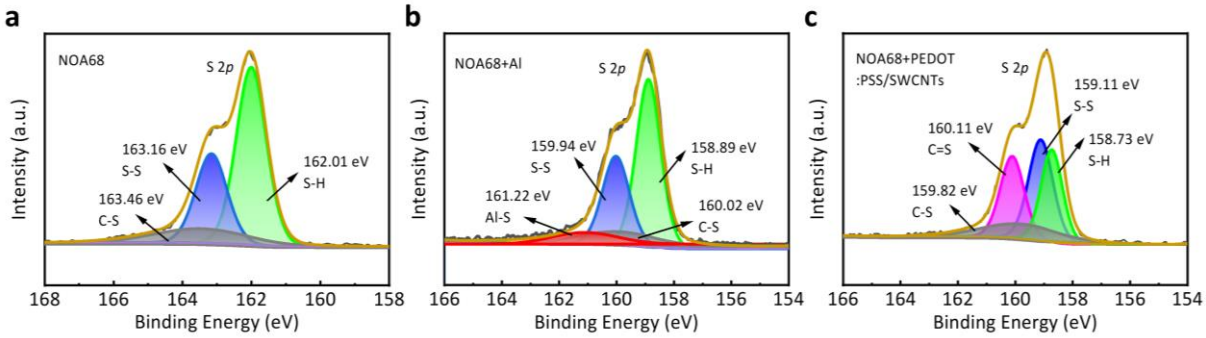

Supplementary Fig. S3 | High-resolution XPS spectra of S 2*p*. **a** NOA68. **b** NOA68 combined with the Al cathode. **c** NOA68 combined with the PEDOT:PSS/SWCNTs.

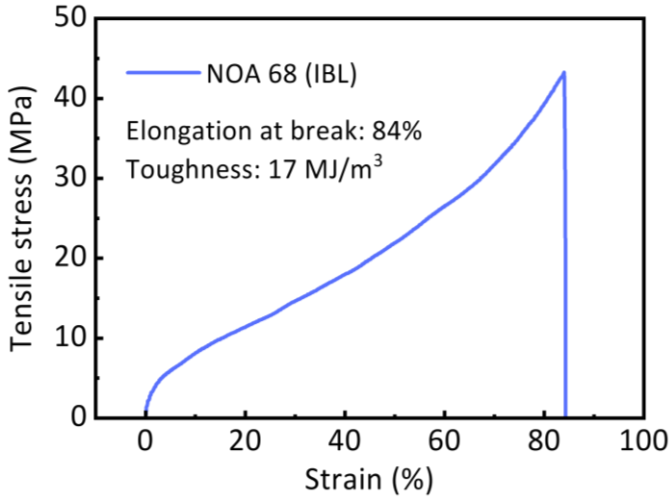

Supplementary Fig. S4 | Stress–strain curve of NOA68 (IBL).

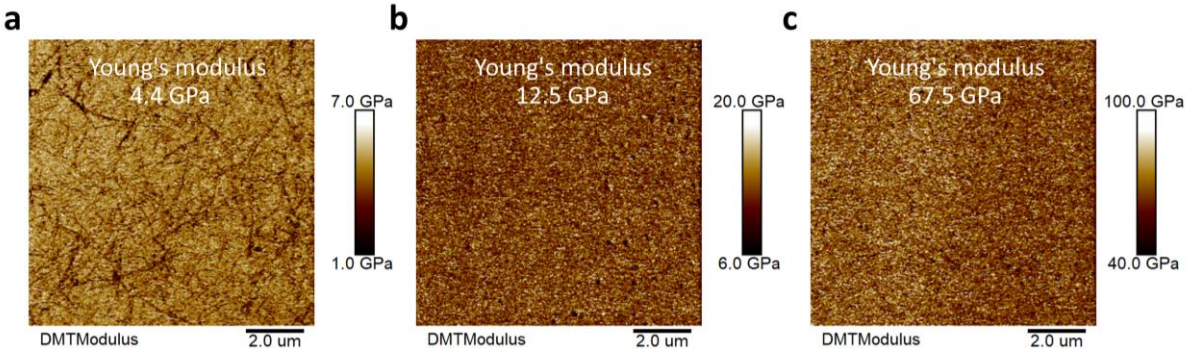

Supplementary Fig. S5 | AFM images of Young's modulus. a PEDOT:PSS/SWCNTs. **b** Active layer. **c** Al.

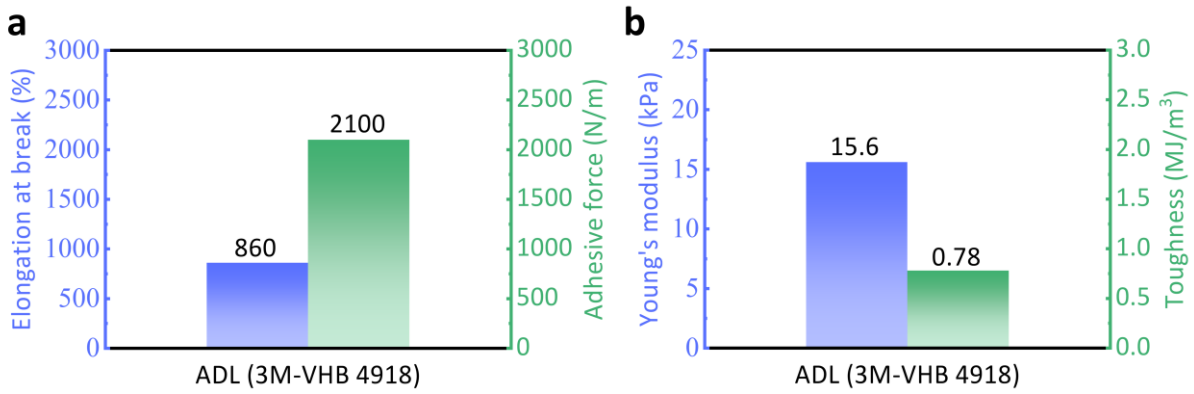

Supplementary Fig. S6 | Mechanical properties of the ADL (3M-VHB 4918). a Elongation at break and adhesive force. **b** Young's modulus and toughness.

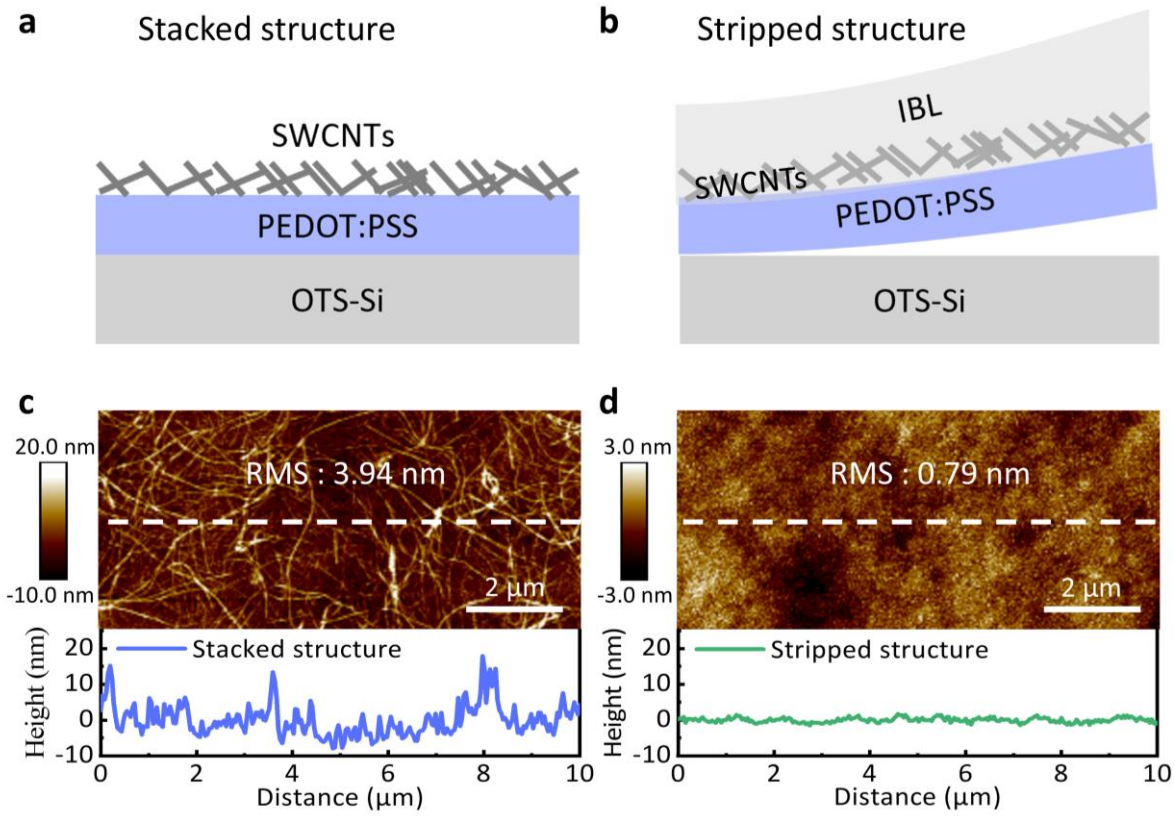

Supplementary Fig. S7 | Comparison of peeling-assisted and conventional stacked strategies for PEDOT:PSS/SWCNTs anodes. a, b Schematic diagrams of the stacked (**a**) and stripped PEDOT:PSS/SWCNTs anodes (**b**). **c, d** AFM surface morphologies of the stacked (**c**) and stripped PEDOT:PSS/SWCNTs anodes (**d**).

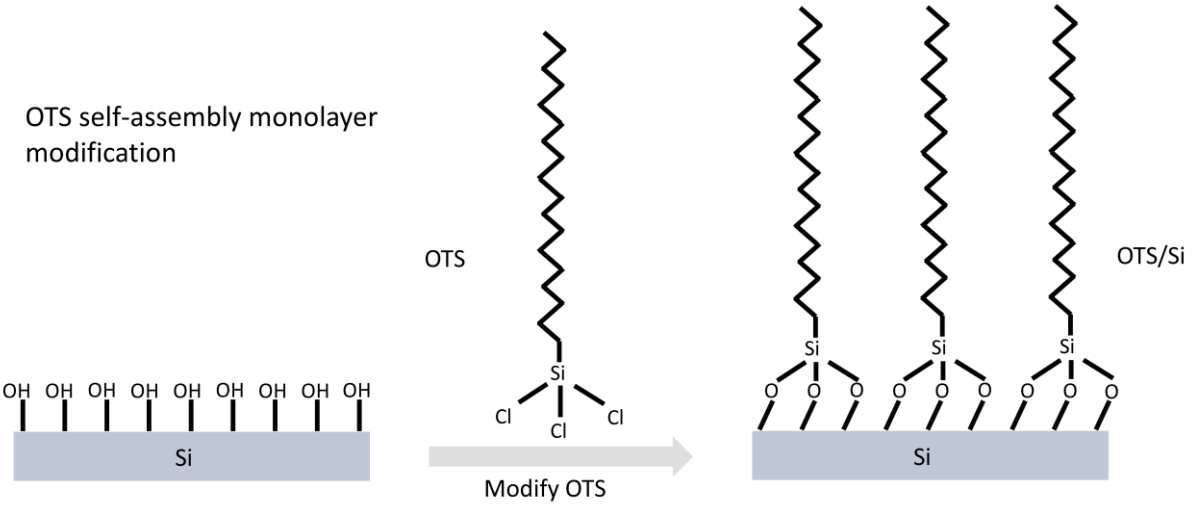

Supplementary Fig. S8 | Schematic diagram of OTS self-assembled monolayer modification.

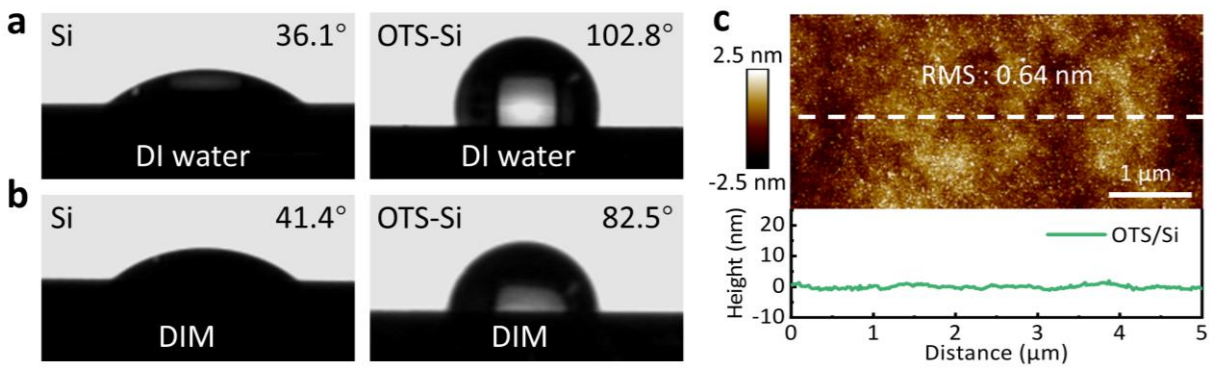

Supplementary Fig. S9 | Contact angle images of DI water and DIM on Si (**a**) and OTS/Si (**b**) substrates, and AFM surface morphology of the OTS/Si substrate (**c**).

Supplementary Fig. S10 | Photographs of the embedded anode peeled from the OTS/Si substrate (**a**), and changes in the sheet resistance of the anode before and after peeling (**b**).

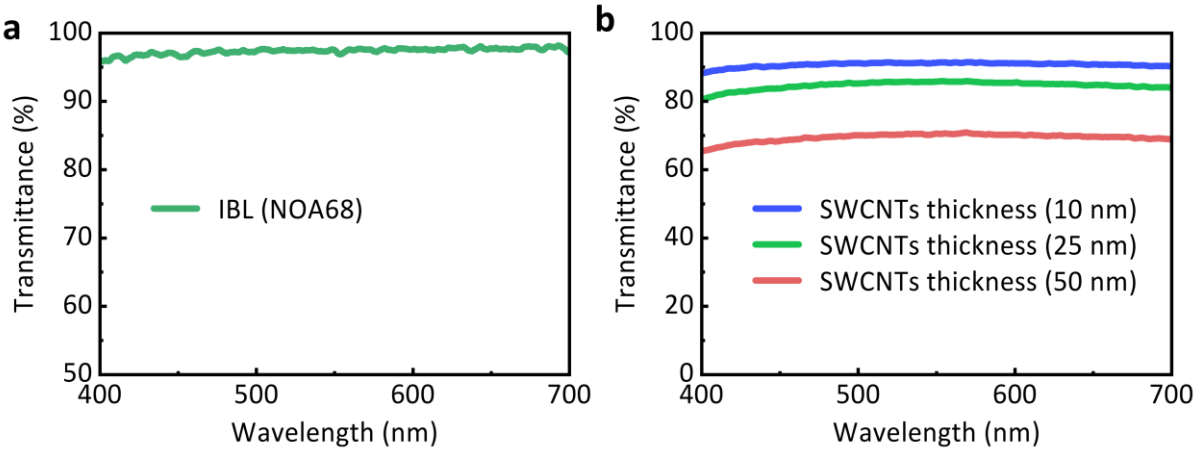

Supplementary Fig. S11 | Transmittance spectrum of the IBL (**a**) and the PEDOT:PSS/SWCNTs electrodes with different SWCNTs thicknesses of 10, 25, and 50 nm (**b**).

We first measured the optical transmittance of the IBL. The IBL exhibits a high transmittance of 97.5% at 550 nm and an average transmittance of 97.4% in the visible region (Supplementary Fig. 11a), indicating that embedding the electrode within the IBL does not significantly compromise the optical transparency. Subsequently, the transmittance of PEDOT:PSS/SWCNTs composite electrodes with different SWCNTs thicknesses was evaluated. For SWCNT thicknesses of 10, 25, and 50 nm, the average visible transmittance values are 90.8%, 84.7%, and 69.4%, respectively, while the corresponding transmittance values at 550 nm are 91.3%, 85.8%, and 70.6% (Supplementary Fig. 11b). The corresponding sheet resistances are 238, 92, and 49 Ω/sq, respectively. To obtain the optimal conditions for the composite anode, the figure of merit (FOM), defined as $FOM = \frac{\eta_{dc}}{\eta_{opt}} = \frac{188.5}{Rs(\frac{1}{\sqrt{T}}-1)}$ to trade-off conductivity and transmittance. Here, η_{dc} and η_{opt} stand for the electrical conductivity and optical conductivity of the PEDOT:PSS/SWCNTs composite film. R_s and T stand for sheet resistance and transmittance at 550 nm. The calculated FOM values for the electrodes with 10, 25, and 50 nm SWCNTs are 17.0, 25.7, and 20.2, respectively. Therefore, the PEDOT:PSS/SWCNTs electrode with 25 nm SWCNTs was selected as the optimized condition, as it exhibits the highest FOM and thus provides the optimal balance between transparency and conductivity. Based on this optimized electrode, which consists of a 15 nm-thick PEDOT:PSS layer and a 25 nm-thick SWCNT layer with a total thickness of 40 nm, the electrical conductivity was further calculated by $\sigma = \frac{1}{R_{sq} \times n}$, where R_{sq} is the sheet resistance and n is the film thickness. With a sheet resistance of 92 Ω/sq, the optimized transparent anode shows a high electrical conductivity of 2717 S/cm.

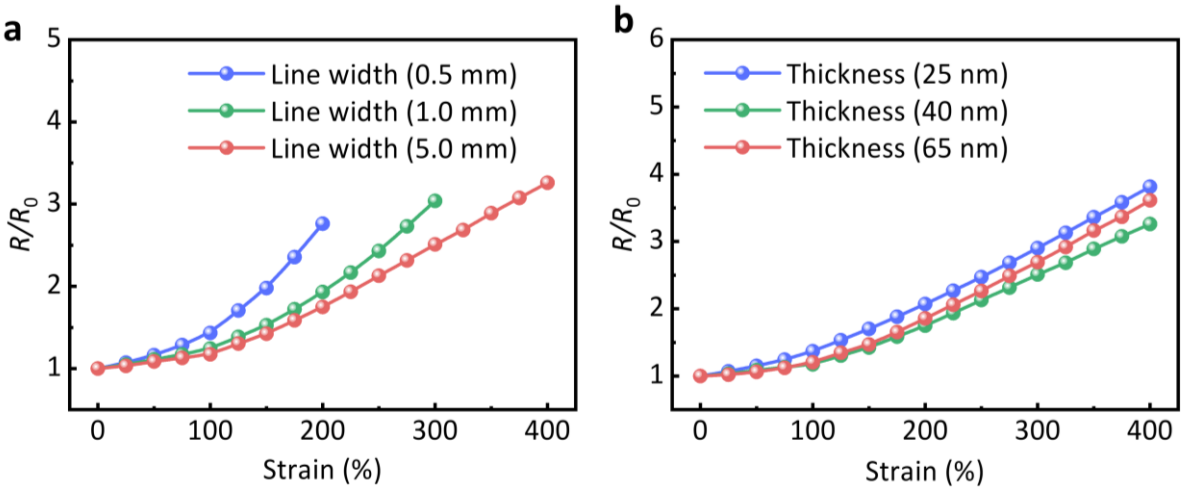

Supplementary Fig. S12 | Mechanical stability of PEDOT:PSS/SWCNT electrodes under tensile strains ranging from 0 to 400%. a Normalized resistance changes (R/R_0) of electrodes with different line widths of 0.5, 1.0, and 5.0 mm as a function of tensile strains. **b** Normalized resistance changes of electrodes with different thicknesses of 25, 40, and 65 nm under tensile strains.

To evaluate the influence of electrode width on stretchability, we fabricated PEDOT:PSS/SWCNTs electrodes with different line widths. As shown in Supplementary Fig. 12a, the line width of the electrode affects the resistance stability under different tensile strains. Compared with narrower electrodes, the 5.0 mm-wide electrode exhibits a smaller increase in normalized resistance and can withstand tensile strains up to 400%, which can be attributed to more effective stress dispersion and more abundant conductive pathways within the wider electrode. The influence of total electrode thickness was further investigated. As revealed in Supplementary Fig. 12b, the 40 nm-thick electrode exhibits the lowest normalized resistance variation. For the thinner electrode, the conductive SWCNTs network may be insufficiently connected, resulting in a relatively larger resistance increase during stretching. In contrast, the 40 nm-thick electrode forms a more continuous conductive network that can accommodate tensile deformation through nanotube sliding and conductive-pathway reconstruction. Further increasing the total electrode thickness to 65 nm does not further improve the resistance stability, possibly due to the formation of an overly dense network and non-uniform internal stress distribution under tensile deformation. Therefore, the 40 nm-thick PEDOT:PSS/SWCNTs electrode was selected as the optimized transparent stretchable anode.

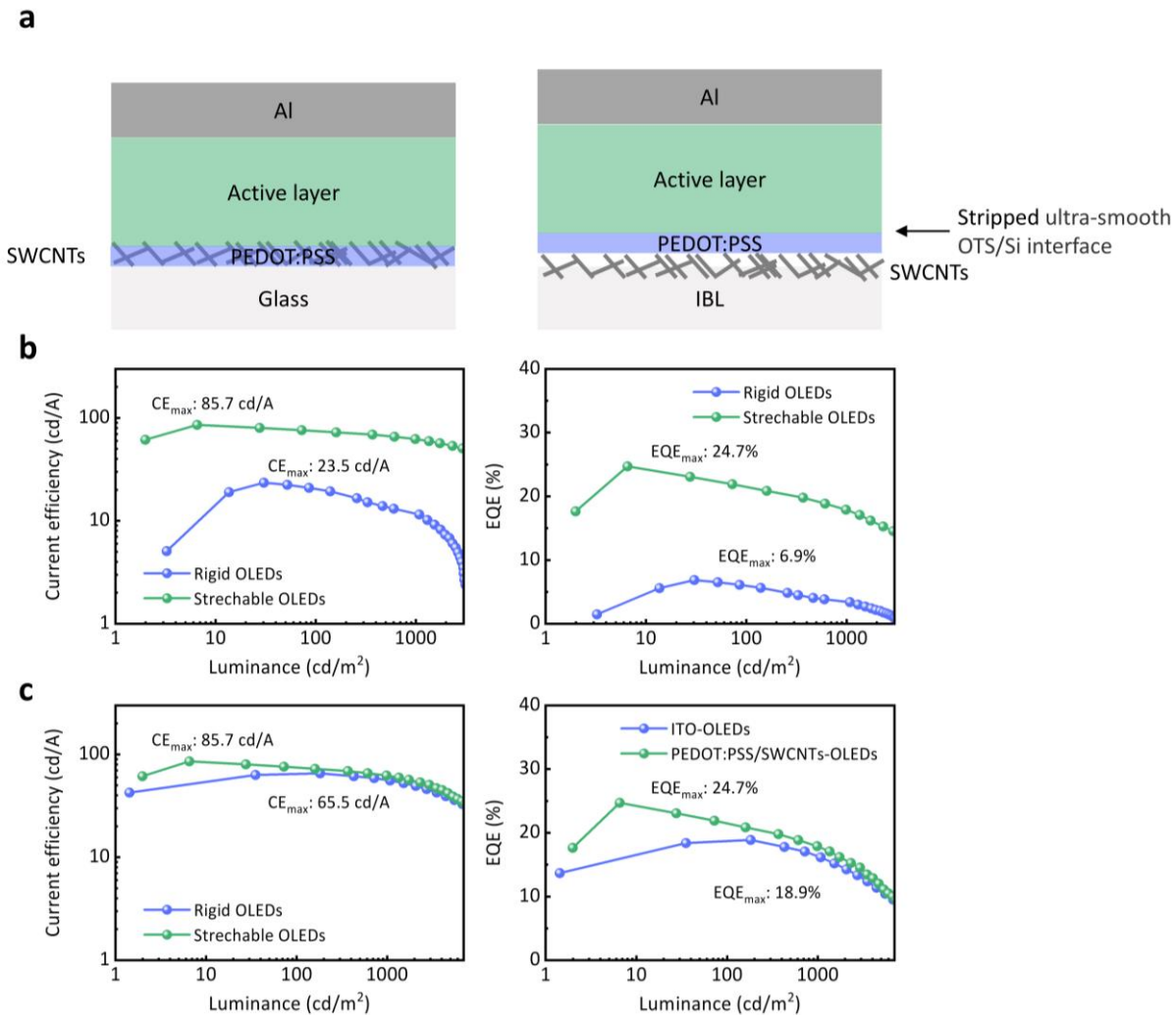

Supplementary Fig. S13 | Comparison of fully stretchable OLEDs with rigid OLEDs based on the same material system. a Schematic illustration of the conventional rigid OLED with a stacked PEDOT:PSS/SWCNTs anode and the fully stretchable OLED with an embedded PEDOT:PSS/SWCNTs anode peeled from the ultra-smooth OTS/Si interface. In the conventional rigid device, the PEDOT:PSS film conforms closely to the underlying SWCNTs network, forming a highly undulating surface. In contrast, the peeled embedded electrode provides a smoother PEDOT:PSS-dominated surface for organic layer deposition. **b** Current efficiency–luminance and EQE–luminance characteristics of the conventional rigid PEDOT:PSS/SWCNTs-based OLED and the fully stretchable OLED. **c** Current efficiency–luminance and EQE–luminance characteristics of the rigid ITO-based OLED and the fully stretchable PEDOT:PSS/SWCNTs-based OLED with the same active layer and cathode. The fully stretchable OLED exhibits higher efficiency than the rigid ITO-based OLED, owing to the improved surface morphology and favorable work-function matching of the embedded PEDOT:PSS/SWCNTs electrode.

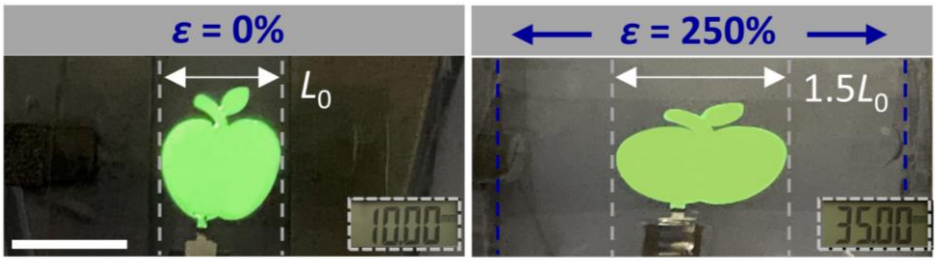

Supplementary Fig. S14 | Photographs of the stretchable OLED under tensile strains of 0% and 250%. The device maintains stable operation under a large tensile strain of up to 250%, corresponding to a 250% expansion of the total electrode area and ≈50% elongation of the emissive region from L_0 to approximately $1.5L_0$, while retaining uniform brightness without significant degradation.

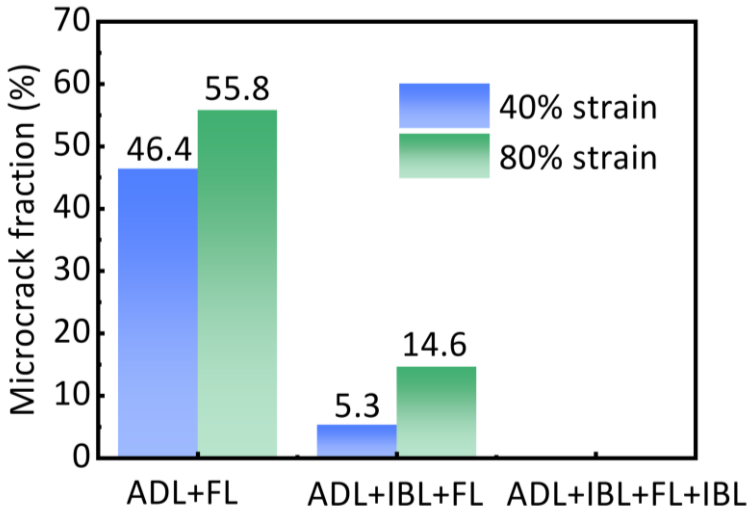

Supplementary Fig. S15 | The area fraction of microcracks in three device structures under different strain levels.

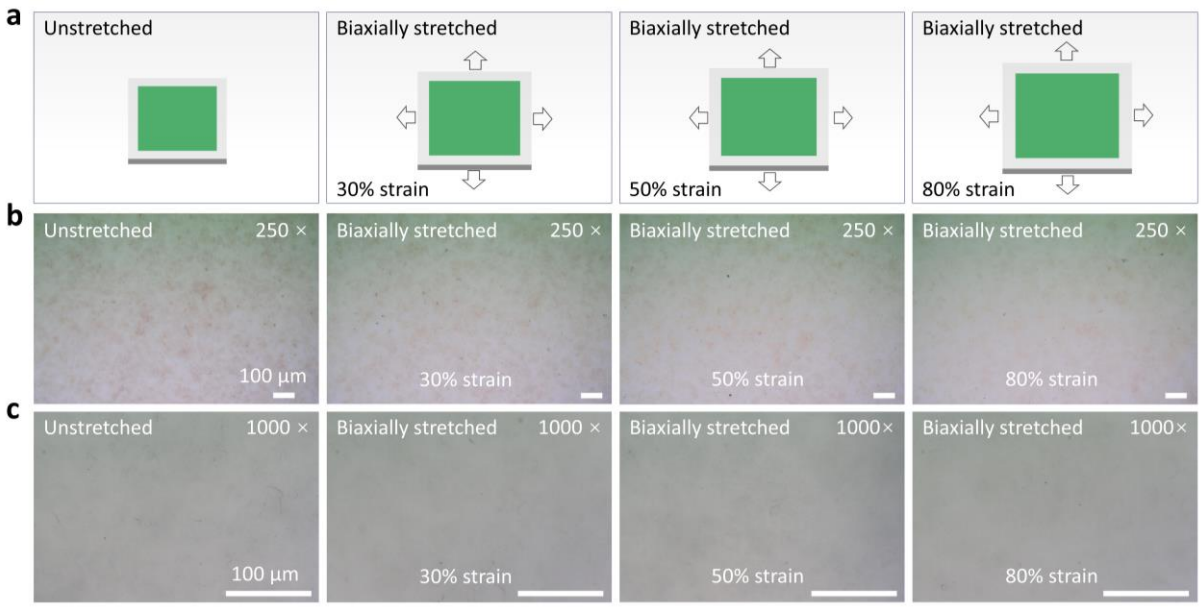

Supplementary Fig. S16 | Surface morphology of the device under different biaxial tensile strains. a Schematic illustrations of the device in the unstretched state and under biaxial stretching at 30%, 50%, and 80% strain. **b**, **c** 3D optical microscopy images of the device in the unstretched state and under biaxial stretching at 30%, 50%, and 80% strain, observed at magnifications of 250× (**b**) and 1000× (**c**), respectively. Scale bars, 100 μm. No obvious surface microcracks or visible damage are observed under biaxial stretching. Representative images are shown; similar results were obtained from three independent experiments.

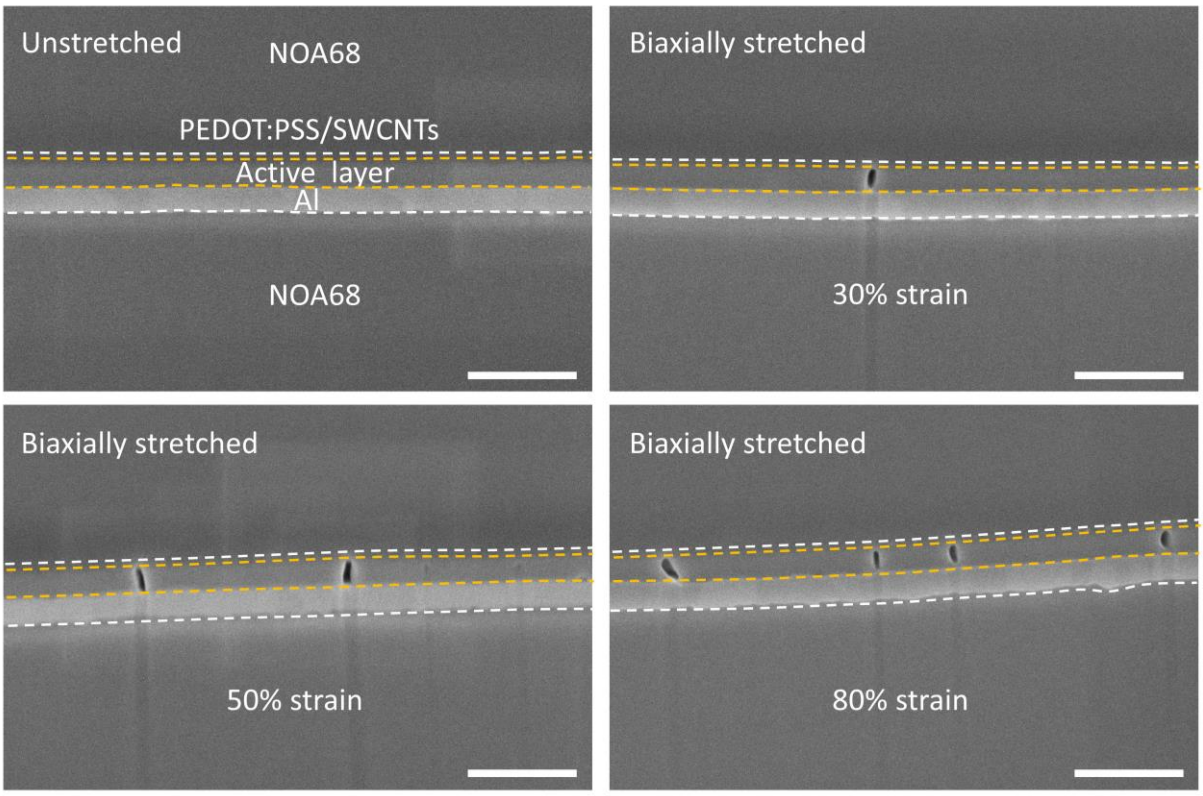

Supplementary Fig. S17 | Cross-sectional FIB-SEM images of the device in the unstretched state and under biaxial stretching at 30%, 50%, and 80% strain. Scale bar, 500 nm. Localized nanocracks are confined within the active layer without propagating through the entire device stack. Representative images are shown; similar results were obtained from three independent experiments.

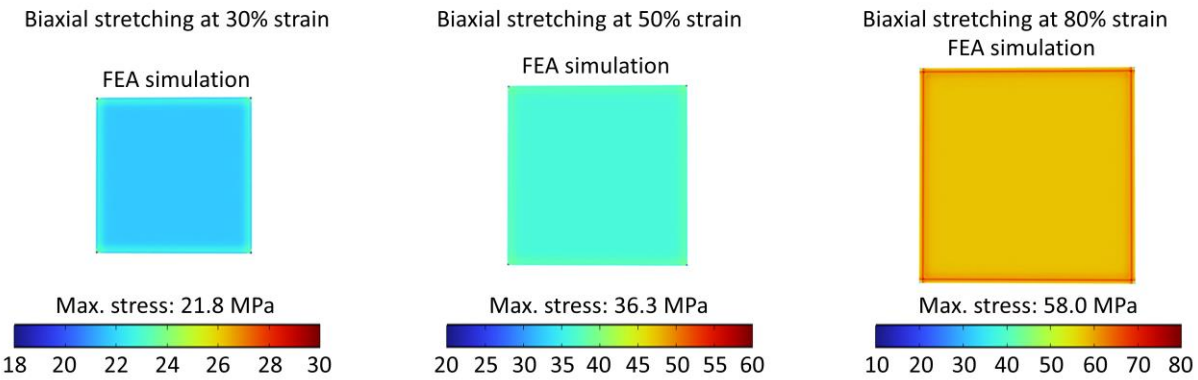

Supplementary Fig. S18 | Finite element analysis of stress distribution under biaxial stretching at 30%, 50%, and 80% strain. The maximum stress increases from 21.8 to 36.3 and 58.0 MPa as the biaxial strain increases from 30% to 50% and 80%, respectively.

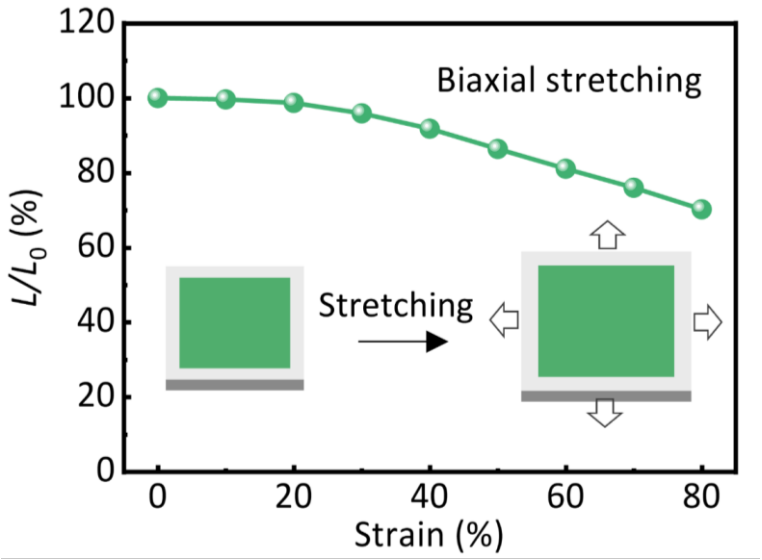

Supplementary Fig. S19 | Normalized luminance changes of the device as a function of biaxial tensile strain.

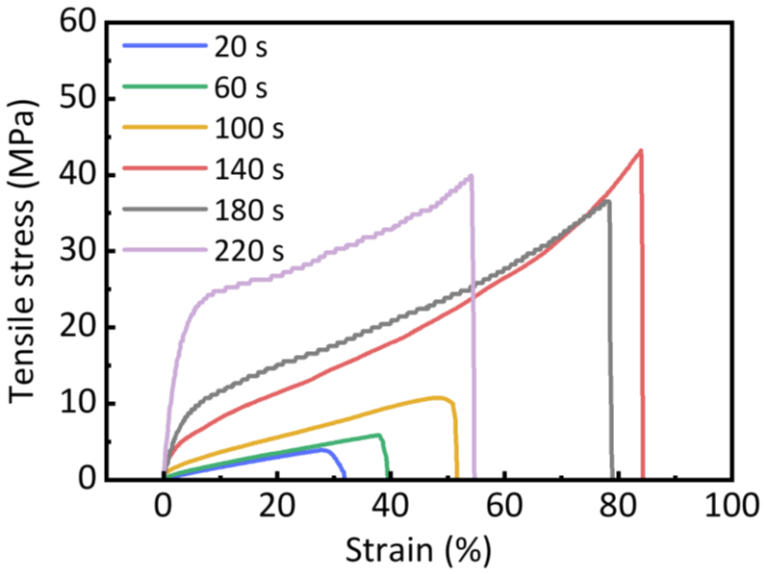

Supplementary Fig. S20 | Stress–strain curves of IBL under different UV irradiating times.

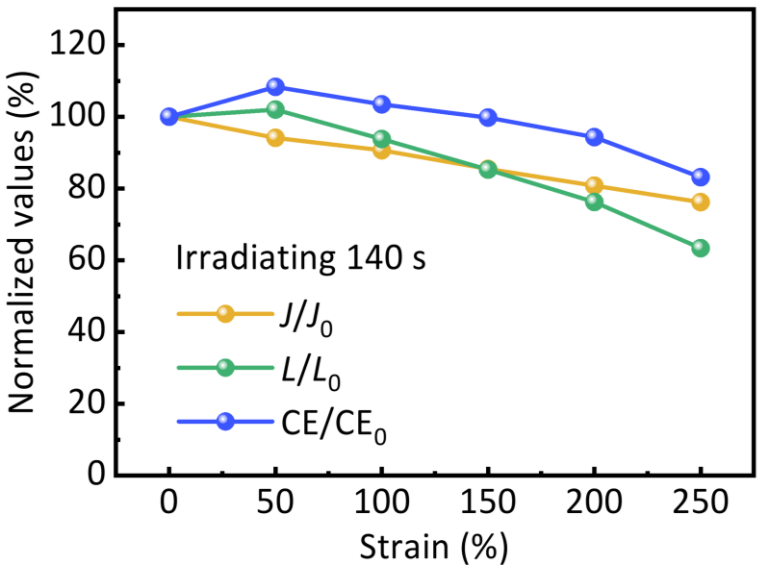

Supplementary Fig. S21 | Normalized current density, luminance, and current efficiency of the ns-OLED with an IBL irradiating time of 140 s as a function of tensile strain.

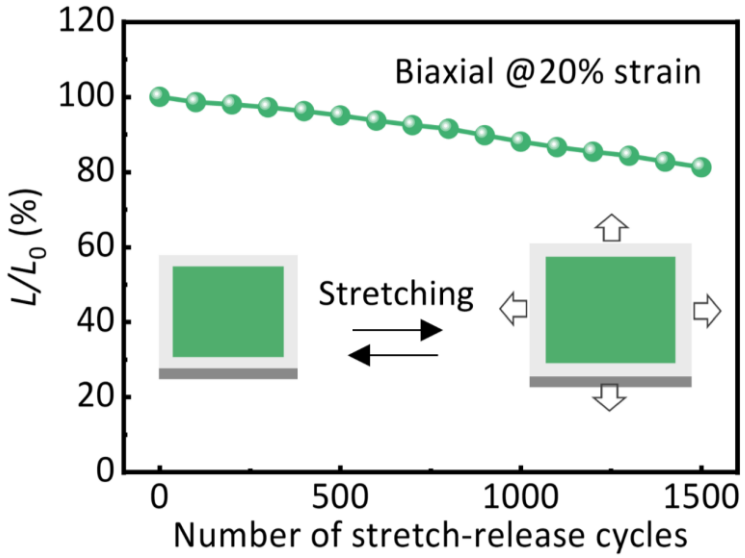

Supplementary Fig. S22 | Normalized luminance variation of the device during repeated stretch–release cycles under biaxial stretching at 20% strain.

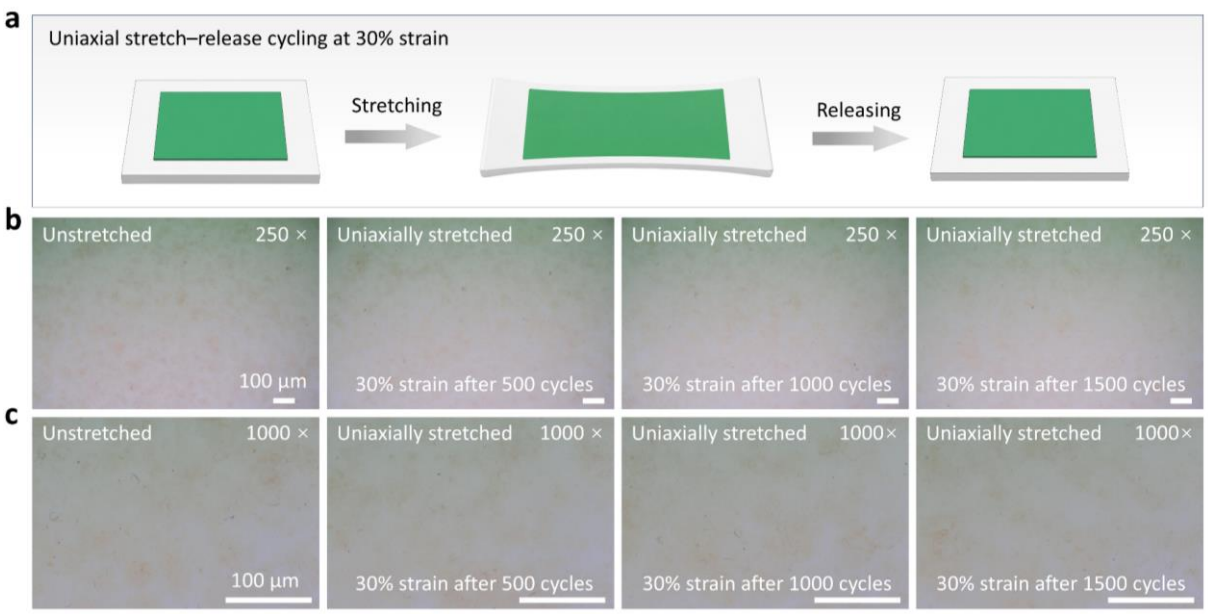

Supplementary Fig. S23 | Surface morphology of the device after repeated uniaxial stretch–release cycles at 30% strain. a Schematic illustration of the uniaxial stretch–release process. **b**, **c** 3D optical microscopy images of the device surface in the pristine state and after 500, 1,000, and 1,500 uniaxial stretch–release cycles at 30% strain, observed at low (**b**) and high magnifications (**c**), respectively. Scale bars, 100 µm. The observed surface features mainly originate from the PEDOT:PSS/SWCNTs electrode morphology, and no obvious surface microcracks, macroscopic crack propagation, or visible damage are observed after cyclic stretching. Representative images are shown; similar results were obtained from three independent experiments.

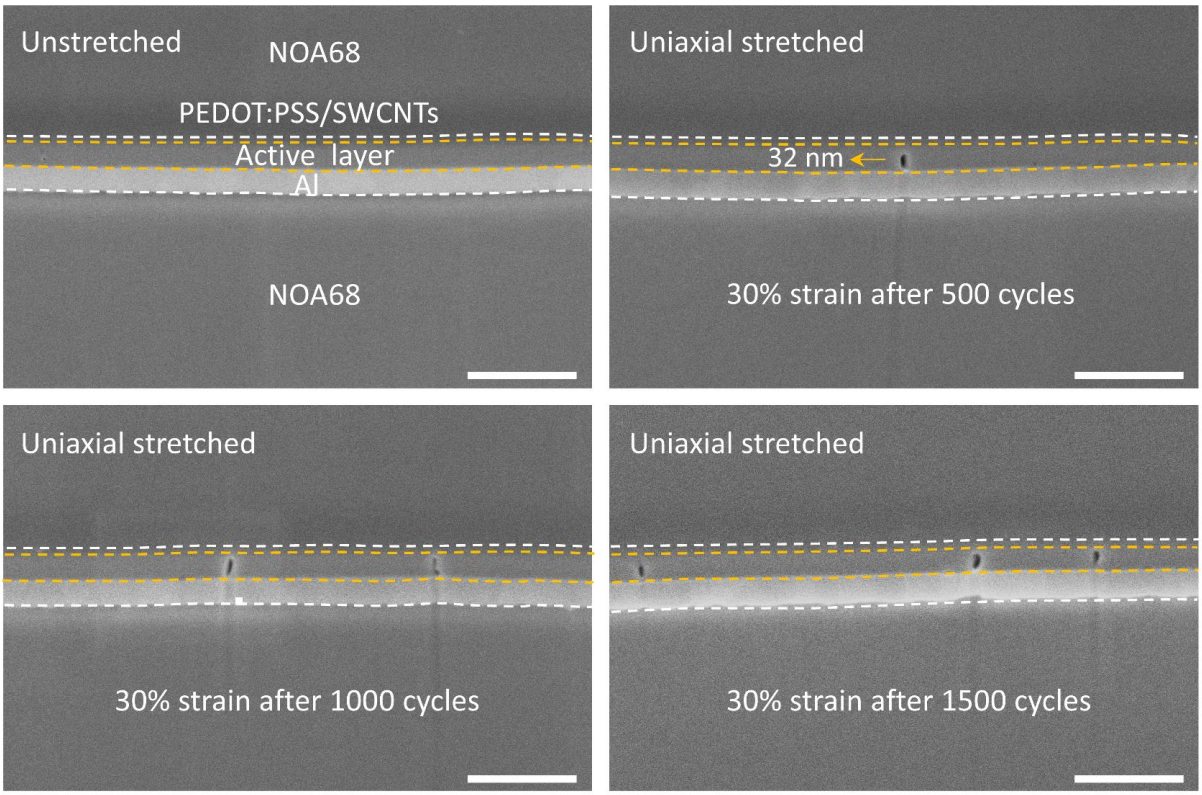

Supplementary Fig. S24 | Cross-sectional FIB-SEM images of the device after 500, 1,000, and 1,500 uniaxial stretch–release cycles at 30% strain. Scale bar, 500 nm. The nanocracks remain localized within the active layer without evolving into through-layer microcracks or inducing obvious interfacial delamination, demonstrating the controlled crack evolution during repeated deformation. Representative images are shown; similar results were obtained from three independent experiments.

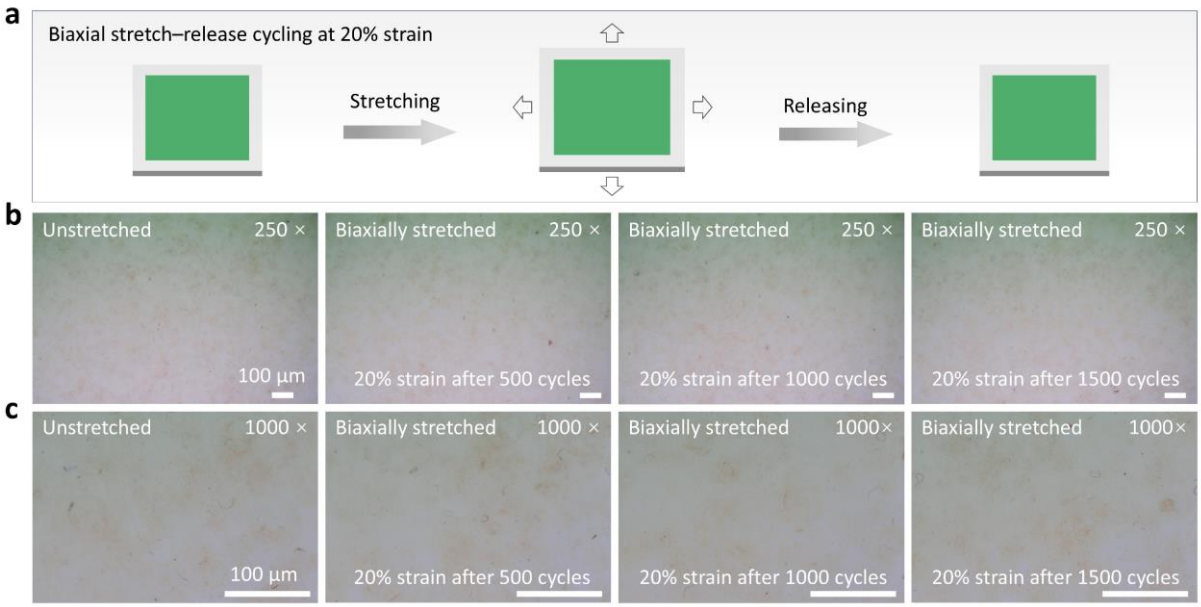

Supplementary Fig. S25 | Surface morphology of the device after repeated biaxial stretch–release cycles at 20% strain. a Schematic illustration of the biaxial stretch–release process. **b**, **c** 3D optical microscopy images of the device surface in the pristine state and after 500, 1,000, and 1,500 biaxial stretch–release cycles at 20% strain, observed at low (**b**) and high magnifications (**c**), respectively. Scale bars, 100 µm. The observed surface features mainly originate from the PEDOT:PSS/SWCNTs electrode morphology, and no obvious surface microcracks are observed after cyclic stretching. Representative images are shown; similar results were obtained from three independent experiments.

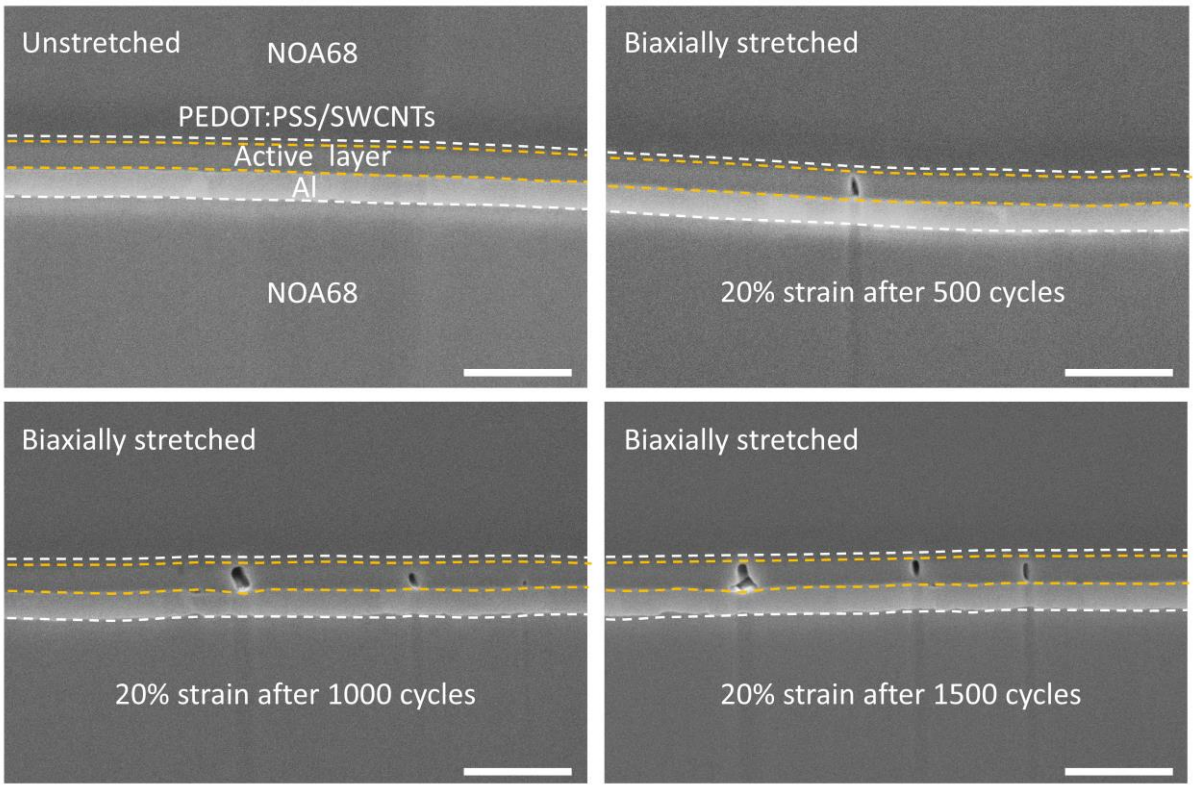

Supplementary Fig. S26 | Cross-sectional FIB-SEM images of the device after 500, 1,000, and 1,500 biaxial stretch–release cycles at 20% strain. Scale bar, 500 nm. The nanocracks remain localized within the active layer without evolving into through-layer microcracks or inducing obvious interfacial delamination, demonstrating the controlled crack evolution during repeated deformation. Representative images are shown; similar results were obtained from three independent experiments.

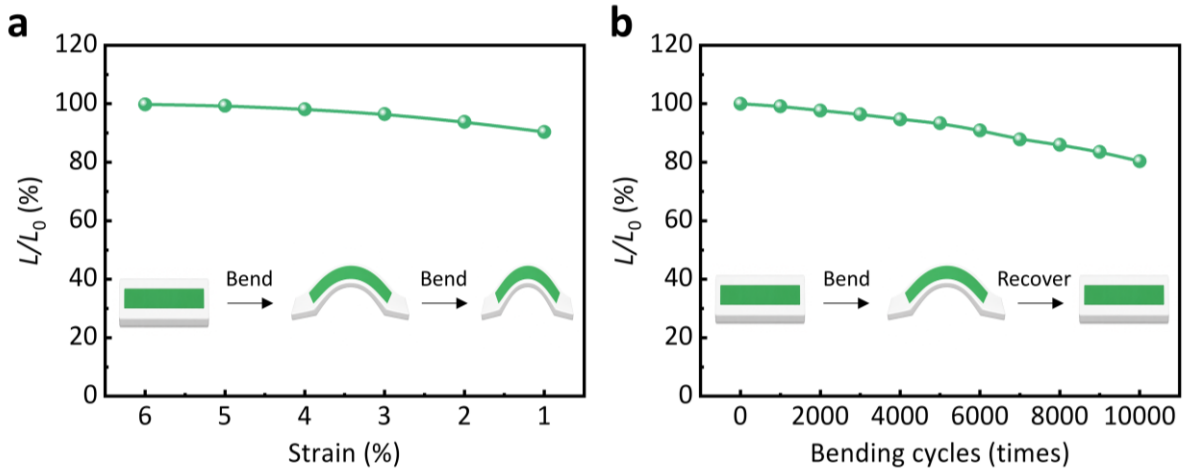

Supplementary Fig. S27 | Bending stability test of stretchable OLEDs. a Normalized luminance variation under progressively reduced bending radii from 6 to 1 mm. **b** Normalized luminance variation under repeated bending–recovery cycles at a bending radius of 5 mm.

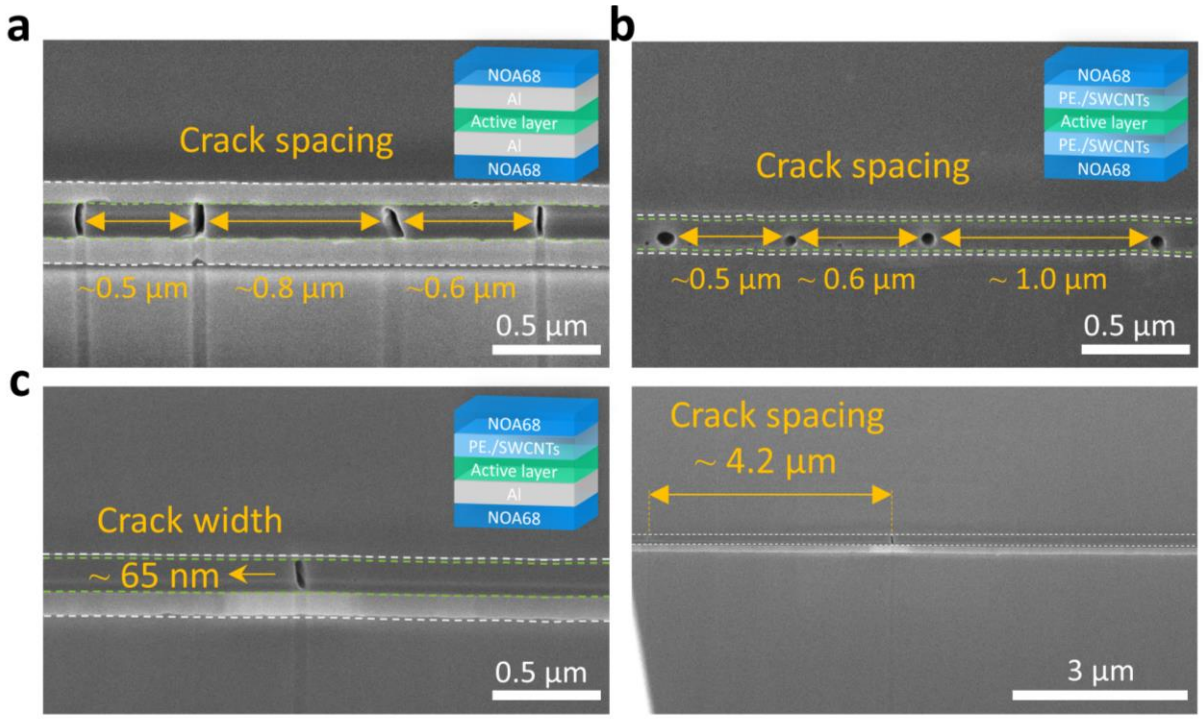

Supplementary Fig. S28 | Crack spacing analysis of different electrodes/active-layer configurations. a FIB-SEM image of the symmetric Al/active layer/Al configuration, showing dense vertically penetrating nanocracks with crack spacings of ≈0.5–0.8 µm. **b** FIB-SEM image of the symmetric PEDOT:PSS/SWCNTs/active layer/PEDOT:PSS/SWCNTs configuration, showing dense cracks with crack spacings of ≈0.5–1.0 µm. **c** High-magnification and low-magnification FIB-SEM images of the asymmetric PEDOT:PSS/SWCNTs/active layer/Al configuration, showing a nanocrack width of ≈65 nm and a crack spacing of ≈4.2 µm.

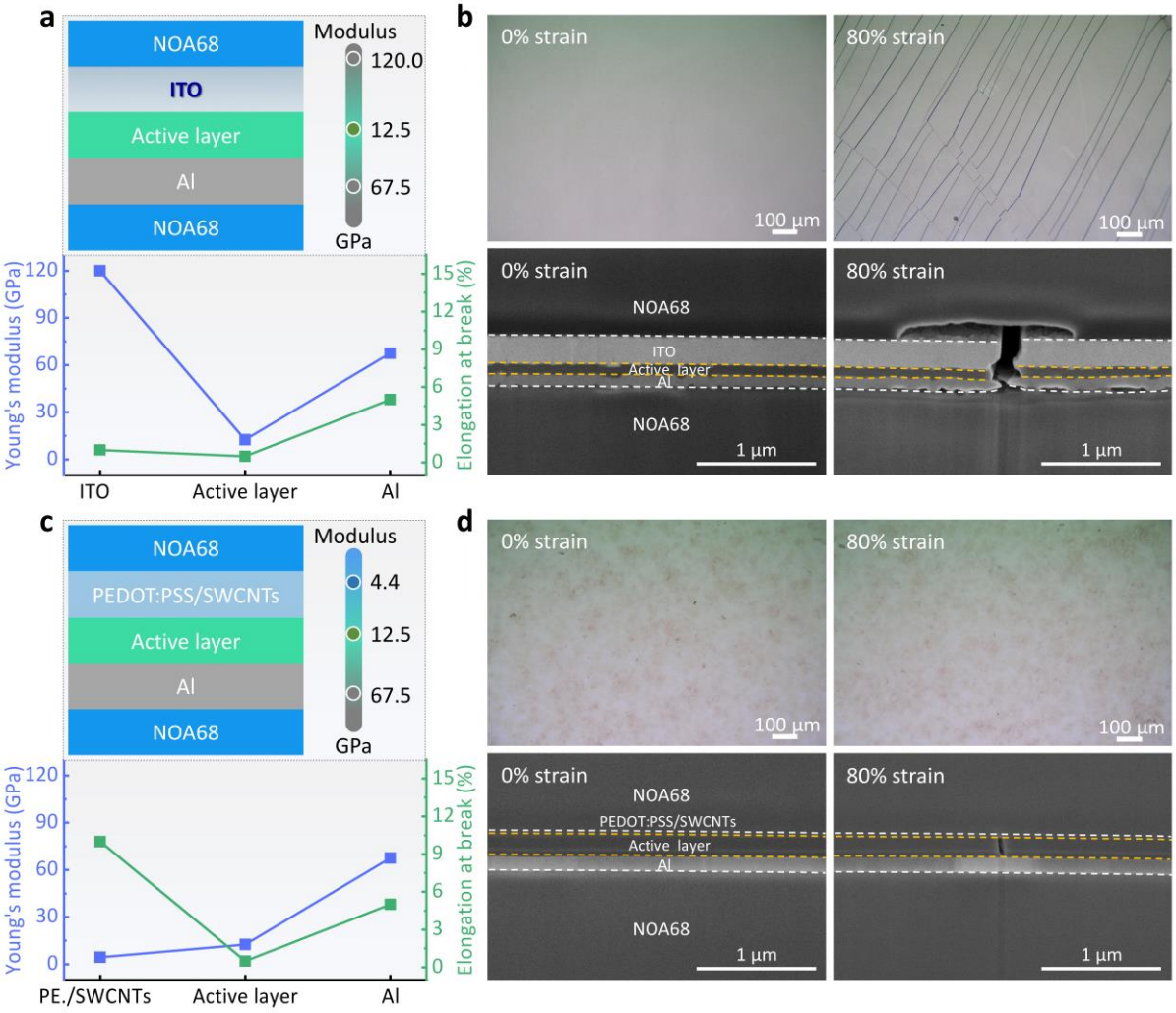

Supplementary Fig. S29 | Comparison of crack evolution in conventional ITO/active layer/Al and asymmetric PEDOT:PSS/SWCNTs/active layer/Al architectures. a Schematic illustration of the conventional ITO/active layer/Al high-modulus configuration and the corresponding Young's modulus and elongation at break. **b** 3D optical microscopy images and cross-sectional FIB-SEM images of the ITO/active layer/Al high-modulus configuration before and after stretching to 80% tensile strain. **c** Schematic illustration of PEDOT:PSS/SWCNTs/active layer/Al asymmetric gradient modulus configuration and the corresponding Young's modulus and elongation at break. **d** 3D optical microscopy images and cross-sectional FIB-SEM images of PEDOT:PSS/SWCNTs/active layer/Al asymmetric gradient modulus configuration before and after stretching to 80% tensile strain.

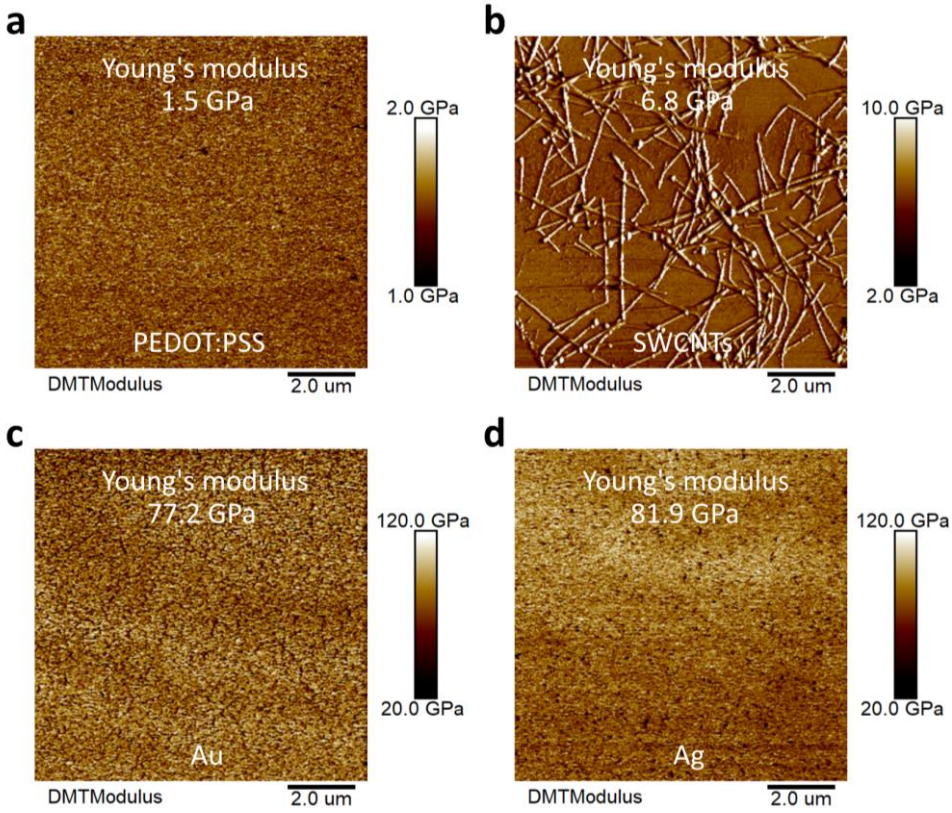

Supplementary Fig. S30 | AFM images of the Young's modulus distributions of PEDOT:PSS (a), SWCNTs (b), Au (c), and Ag (d). The measured Young's moduli of PEDOT:PSS, SWCNTs, Au, and Ag are approximately 1.5, 6.8, 77.2, and 81.9 GPa, respectively.

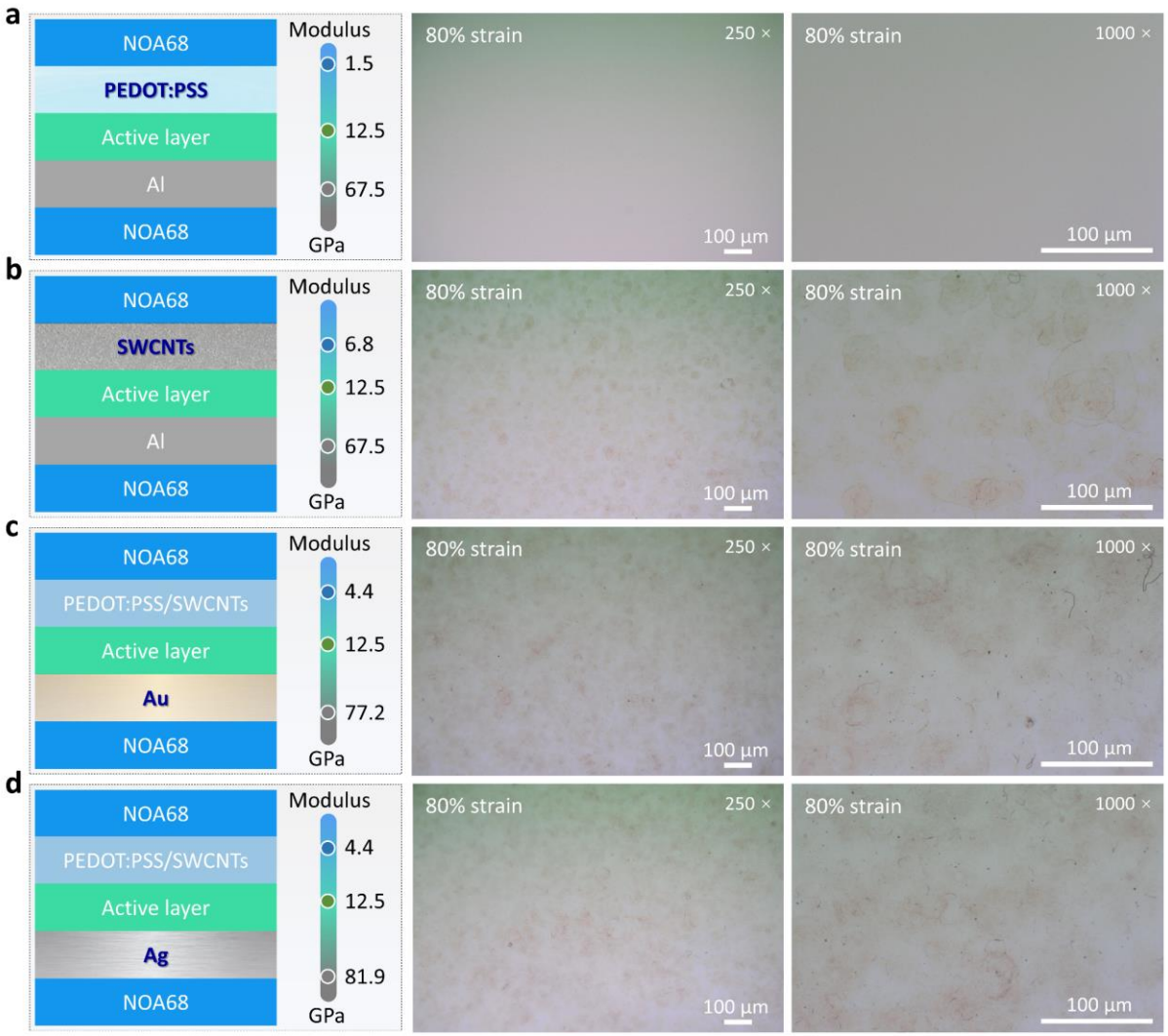

Supplementary Fig. S31 | Layer structures with corresponding modulus distributions and 3D optical microscopy images of devices with different anode/cathode combinations under 80% tensile strain. a, **b** Devices with a fixed Al cathode and different anodes of PEDOT:PSS (**a**) and SWCNTs (**b**), respectively. **c**, **d** Devices with a fixed PEDOT:PSS/SWCNTs composite anode and different cathodes of Au (**c**) and Ag (**d**), respectively. Both low- and high-magnification images show no obvious surface microcracks, macroscopic crack propagation, or severe structural damage. Representative images are shown; similar results were obtained from three independent experiments.

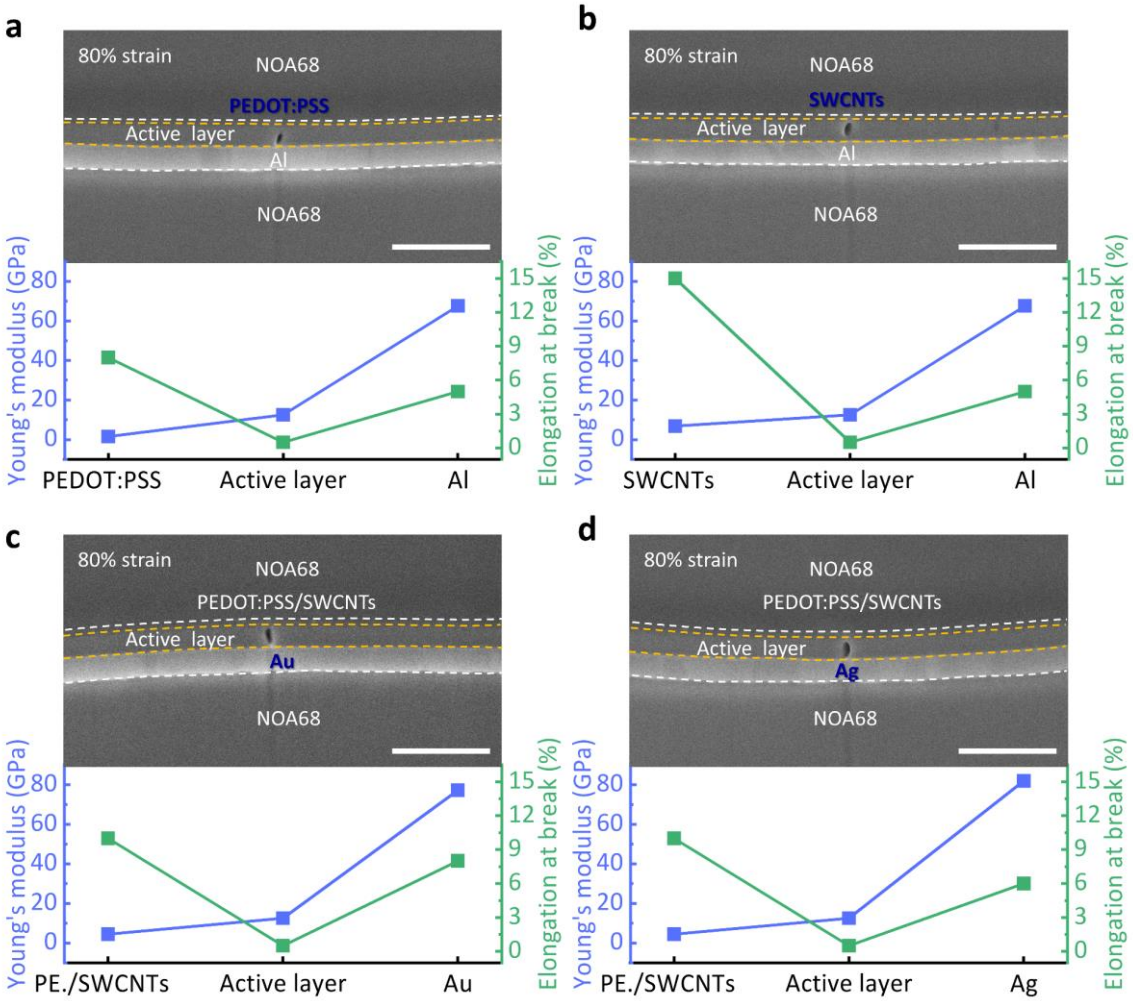

Supplementary Fig. S32 | Cross-sectional FIB-SEM images and corresponding Young's modulus/elongation at break distributions of devices under 80% tensile strain. a, **b** Devices with a fixed Al cathode and different anodes of PEDOT:PSS (**a**) and SWCNTs (**b**), respectively. **c**, **d** Devices with a fixed PEDOT:PSS/SWCNTs composite anode and different cathodes of Au (**c**) and Ag (**d**), respectively. Scale bar, 500 nm. Under 80% tensile strain, the internal cracks remain at the nanoscale and are confined within the active layer, without penetrating through the entire functional stack or developing into large-scale microcracks. Representative images are shown; similar results were obtained from three independent experiments.

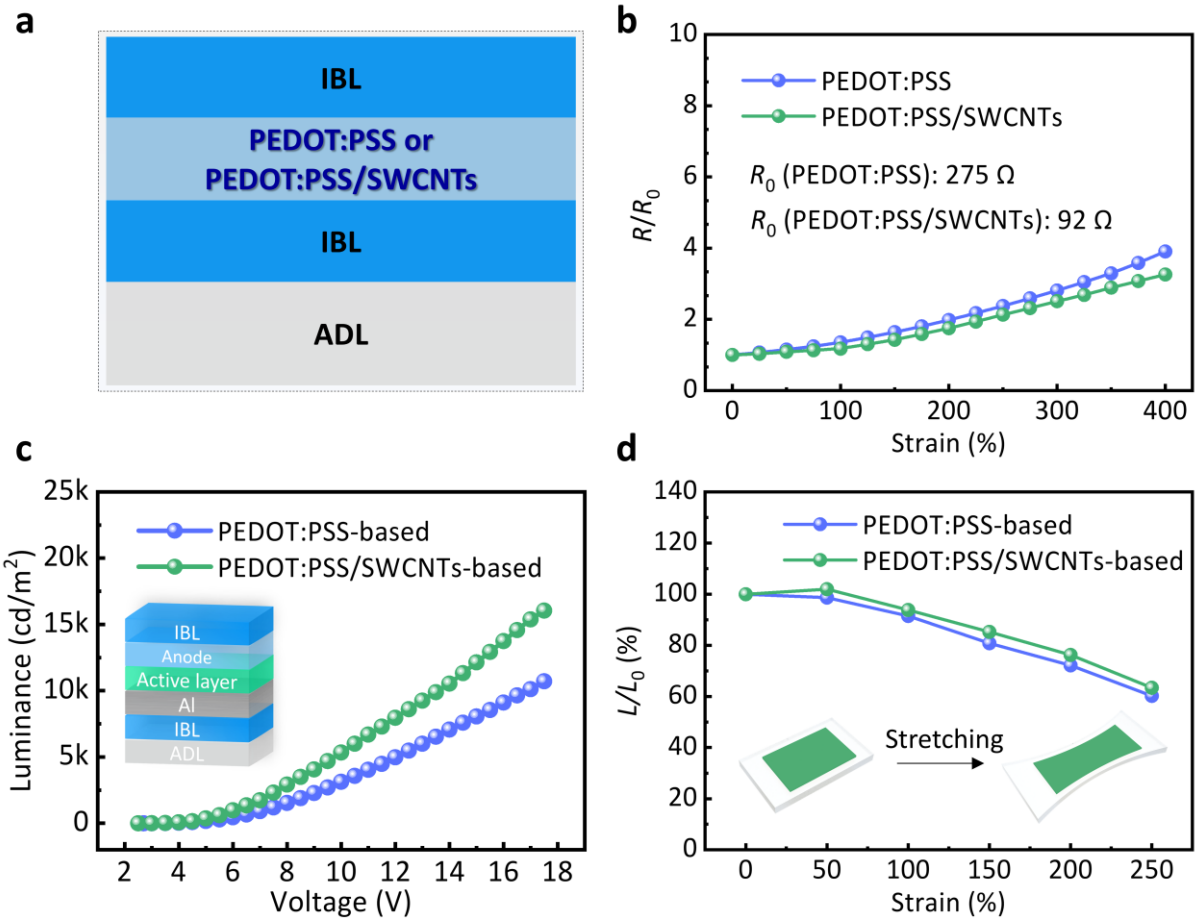

Supplementary Fig. S33 | Comparison of electrical conductivity, optoelectronic performance, and mechanical stability between PEDOT:PSS and PEDOT:PSS/SWCNTs electrodes and corresponding devices. a Schematic structure of the device using PEDOT:PSS or PEDOT:PSS/SWCNTs as the anode. **b** Normalized resistance variation of PEDOT:PSS and PEDOT:PSS/SWCNTs electrodes under different tensile strain. **c** Luminance–voltage characteristics of PEDOT:PSS- and PEDOT:PSS/SWCNTs-based devices. **d** Normalized luminance variation of the corresponding devices under different tensile strains.

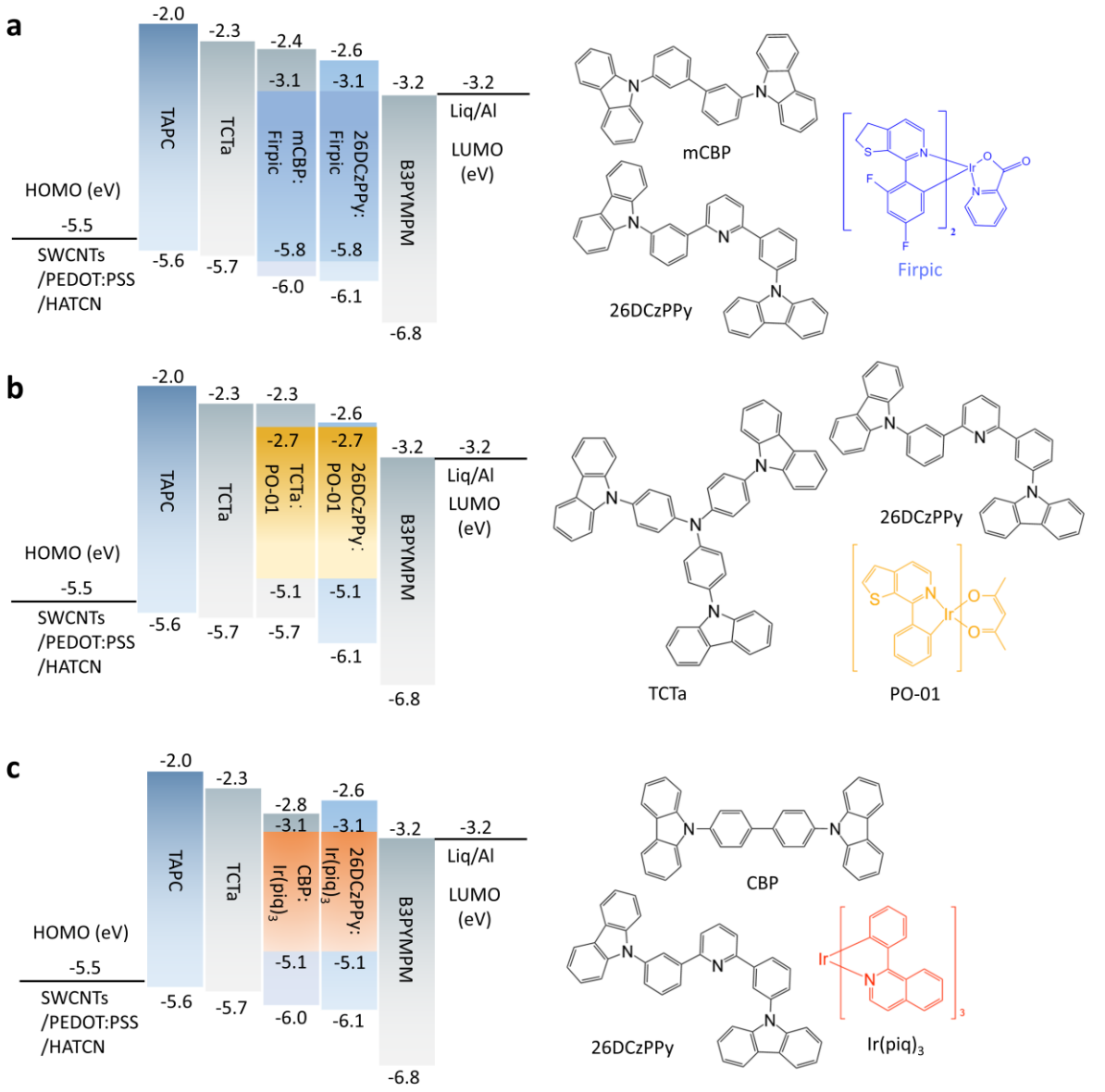

Supplementary Fig. S34 | Energy-level alignment diagram of fully stretchable SMOS-OLEDs with different colors and the molecular structures of the corresponding emissive materials. Blue (**a**), yellow (**b**), and red **(c)** emission.

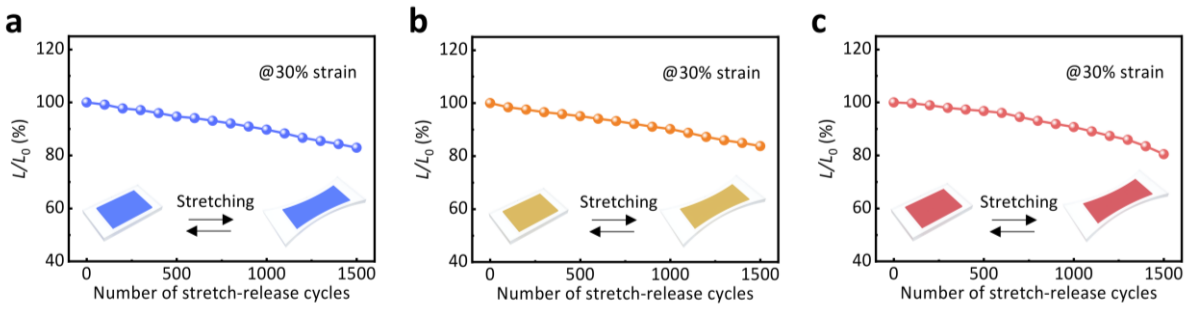

Supplementary Fig. S35 | Normalized luminance variation of the three devices during repeated uniaxial stretch–release cycles at 30% strain. a Blue-emitting device. **b** Yellow-emitting device. **c** Red-emitting device.

Supplementary Table S1 | Comparison of this study with recently reported stretchable LEDs, including organic, polymer, QD, and perovskite LEDs.

Device category	Emissive material	Maximum stretchability (%)	Stretching cycle (times)	Peak CE (cd/A)	Peak brightness (cd/m^2)	V_{on} (V)	*Ref.*
Island-bridge OLEDs	TCTA/Ir(dmppy-ph)$_2$tmd/B3PYMPM	40	2,000 of 40% strain	≈65.0	>10,000	-	[2]
	Alq_3	40	1,000 of 40% strain	-	2,000	2.5	[3]
	Alq_3	35	1,000 of 20% strain	3.0	2,000	4	[4]
	TTPA	50	-	-	364	7	[5]
Buckling OLEDs	$Ir(ppy)_3$	80	100 of 25% strain	71.0	9,699	3	[6]
	$Ir(ppy)_3$	100	15,000 of 100% strain	70.0	11,000	3	[7]
	$Ir(BT)_2(acac)$	100	20,000 of 20% strain	73.0	-	-	[8]
	$Ir(ppy)_3$	100	35,000 of 20% strain	66.0	15,110	-	[9]
	PO-01/Firpic	100	-	77.0	34,787	2.9	[10]
Buckling PLEDs	PPE-PPV	100	2 of 100% strain	0.026	113	<5	[11]
	Conjugated polymer system	200	1,000 of 60% strain	-	4,900	-	[12]
	PDY-132	20	1,000 of 10% strain	7.8	8,000	2.4	[13]
Buckling QLEDs	CdSe-CdS-ZnS QDs	70	100 of 70% strain	2.3	1,310	2.8	[14]
	CdSe-ZnS QDs	50	-	17.5	43,000	3	[15]
	$CH3NH3PbBr_3$ QDs	50	1,000 of 20% strain	9.2	3,187	3.2	[16]
Textile OLEDs	$Ir(ppy)_2acac$	20	-	46.0	4,300	2.3	[17]
Fully stretchable PeACELs	PeZS phosphors	400	500 of 100% strain	-	>200	25	[18]
Fully stretchable ACELs	Nanocomposite	80	1,000 of 50% strain	-	612	10	[19]
Fully stretchable perovskite/polymer LEDs	$CH3NH3PbBr_3$/PEO	40	100 of 40% strain	3.2	15,960	2.4	[20]
Fully stretchable QLEDs	QD (CdSe/ZnS QDs)/SEBS-g-MA	50	200 of 30% strain	5.0	15,170	3.2	[21]
Fully stretchable PLEDs	SY/PEO/ETPTA/LiTf	120	1,000 of 30% strain	11.4	2,200	6.8	[22]
	Emitting polymer/OXD-7	130	100 of 40% strain	4.0	1,100	8	[23]
	SY/Triton X	80	200 of 40% strain	1.6	4,400	8.3	[24]
	L-SY-PPV/PAN	40	50 of 15% strain	8.1	3,780	6.5	[25]
	SY (PDY-132)/TX-dissolved toluene	70	300 of 40% strain	5.4	3,151	6	[26]
	SY/PU	100	100 of 40% strain	5.3	7,450	5	[27]
	PFO/SEBS	100	1,000 of 100% strain	0.6	>1,000	<5	[28]
	SY/PU-PCL	100	100 of 20% strain	13.7	>32,013	3.7	[29]
	GPF/SBS	120	100 of 15% strain	7.99	33,443	-	[30]
	F8BT/Z1	15	100 of 10% strain	2.5	5,314	4.0	[31]
	P1	30 (stretchable EML)	1,000 of 10% strain	0.91	≈1,000	-	[32]

Fully stretchable SMOS-OLEDs	SY/SBS/TX	100	20 of 40% strain	-	3,141	9.1	[33]
	SY/Triton X	60	100 of 40% strain	10.35	17,670	3.0	[34]
	PVK/$Ir(ppy)_3$	100 (stretchable EML)	500 of 60% strain	≈25.3	≈5,400	6	[35]
	HVPB/MCP/CzPXZ	20	100 of 10% strain	37.6	11,022	-	[36]
	TCTA/SEBS/$Ir(mppy)_3$	200 (stretchable EML)	100 of 20% strain (stretchable EML)	57.4	-	4.2	[37]
	$Ir(ppy)_2(acac)$/TCTA/TPBi/PU	60	100 of 20% strain	47.9	4,840	<5	[38]
Fully stretchable TADF-OLEDs	PDKCD/PDKCH/PDKCP/PDKCM	60	100 of 100% strain (stretchable EML)	10.2	-	4.75	[39]
	PDKCH	80	100 of 20%/30% strain	25.3	>1,000	3.5	[40]
	PDKCE/DOP	60	-	<2	≈2,500	-	[41]
Our work	$Ir(ppy)_3$/$Ir(piq)_3$/PO-01/Firpic	250	1,500 of 30% strain	85.7	16,050	2.5	

1

Supplementary Table S2 | Surface energies and their polar and dispersive components of deionized (DI) water and diiodomethane (DIM).

Solvents	γ_{1v}^{p} (mJ/m^2)	γ_{1v}^{d} (mJ/m^2)	γ_{1v} (mJ/m^2)
DI water	51.0	21.8	72.8
DIM	0.0	50.8	50.8

Supplementary Table S3 | Contact angles of DI water and DIM on Si and OTS/Si surfaces and the corresponding polar and dispersive components of surface energy.

Substrates	Contact angles (deg.)		γ^p	γ^d	γ^s
	DI water	DIM	(mJ/m^2)	(mJ/m^2)	(mJ/m^2)
Si	36.11	41.42	26.40	38.89	65.29
OTS/Si	102.83	82.53	1.77	16.22	17.99

Supplementary References

1. Kwok, D. Y. et al. Contact angle measurement and contact angle interpretation. *Adv. Colloid Interface Sci.* **81**, 167–249 (1999).
2. Kim, S. B. et al. 3D height-alternant island arrays for stretchable OLEDs with high active area ratio and maximum strain. *Nat. Commun.* **15**, 7802 (2024).
3. Kim, T. et al. Realizing stretchable OLEDs: a hybrid platform based on rigid island arrays on a stress-relieving bilayer structure. *Adv. Mater. Technol.* **5**, 2000494 (2020).
4. Lim, M. S. et al. Two-dimensionally stretchable organic light-emitting diode with elastic pillar arrays for stress relief. *Nano Lett.* **20**, 1526–1535 (2020).
5. Sekitani, T. et al. Stretchable active-matrix organic light-emitting diode display using printable elastic conductors. *Nat. Mater.* **8**, 494–499 (2009).
6. Yin, D. et al. Two-dimensional stretchable organic light-emitting devices with high efficiency. *ACS Appl. Mater. Interfaces.* **8**, 31166–31171 (2016).
7. Yin, D. et al. Efficient and mechanically robust stretchable organic light-emitting devices by a laser-programmable buckling process. *Nat. Commun.* **7**, 11573 (2016).
8. Yin, D. et al. Mechanically robust stretchable organic optoelectronic devices built using a simple and universal stencil-pattern transferring technology. *Light Sci. Appl.* **7**, 35 (2018).
9. Yin, D. et al. Roller-assisted adhesion imprinting for high-throughput manufacturing of wearable and stretchable organic light-emitting devices. *Adv. Opt. Mater.* **8**, 1901525 (2020).
10. Yao, L. Q. et al. High-efficiency stretchable organic light-emitting diodes based on ultra-flexible printed embedded metal composite electrodes. *InfoMat*. **5**, e12410 (2023).
11. White, M. S. et al. Ultrathin, highly flexible and stretchable PLEDs. *Nat. Photonics.* **7**, 811–816 (2013).
12. Yokota, T. et al. Ultraflexible organic photonic skin. *Sci. Adv.* **2**, e1501856 (2016).
13. Jeong, S. et al. Distortion-free stretchable light-emitting diodes via imperceptible microwrinkles. *Adv. Mater. Technol.* **5**, 2000231 (2020).
14. Kim, T. H. et al. Fully stretchable optoelectronic sensors based on colloidal quantum dots for sensing photoplethysmographic signals. *ACS Nano*. **11**, 5992–6003 (2017).
15. Choi, M. K. et al. Extremely vivid, highly transparent, and ultrathin quantum dot light-emitting diodes. *Adv. Mater.* **30**, 1703279 (2018).
16. Li, Y. F. et al. Stretchable organometal-halide-perovskite quantum-dot light-emitting diodes. *Adv. Mater.* **31**, 1807516 (2019).

17. Song, Y. J. et al. Fibertronic organic light-emitting diodes toward fully addressable, environmentally robust, wearable displays. *ACS Nano*. **14**, 1133–1140 (2020).
18. Chun, F. et al. Multicolour stretchable perovskite electroluminescent devices for user-interactive displays. *Nat. Photonics.* **18**, 856–863 (2024).
19. Guo, H. et al. Stretchable and breathable electroluminescent displays based on ultrathin nanocomposite designs. *Nano Lett.* **24**, 5904–5912 (2024).
20. Bade, S. G. R. et al. Stretchable light-emitting diodes with organometal-halide-perovskite-polymer composite emitters. *Adv. Mater.* **29**, 1607053 (2017).
21. Kim, D. C. et al. Intrinsically stretchable quantum dot light-emitting diodes. *Nat. Electron.* **7**, 365–374 (2024).
22. Liang, J. et al. Elastomeric polymer light-emitting devices and displays. *Nat. Photonics.* **7**, 817–824 (2013).
23. Liang, J. et al. Silver nanowire percolation network soldered with graphene oxide at room temperature and its application for fully stretchable polymer light-emitting diodes. *ACS Nano*. **8**, 1590–1600 (2014).
24. Kim, J. H. et al. Intrinsically stretchable organic light-emitting diodes. *Sci. Adv.* **7**, eabd9715 (2021).
25. Liu, Y. et al. A self-assembled 3D penetrating nanonetwork for high-performance intrinsically stretchable polymer light-emitting diodes. *Adv. Mater.* **34**, 2201844 (2022).
26. Oh, J. H. et al. Intrinsically stretchable OLEDs with a designed morphology-sustainable layer and stretchable metal cathode. *npj Flex. Electron.* **8**, 43 (2024).
27. Zhang, Z. et al. High-brightness all-polymer stretchable LED with charge-trapping dilution. *Nature.* **603**, 624–630 (2022).
28. Jeong, M. W. et al. Intrinsically stretchable three primary light-emitting films enabled by elastomer blend for polymer light-emitting diodes. *Sci. Adv.* **9**, eadh1504 (2023).
29. Shi, W. et al. Submicron structure confined polymers for high-performance intrinsically stretchable light-emitting diodes. *Adv. Mater.* **38**, e19650 (2026).
30. Lu, Z. et al. Intrinsically stretchable organic light-emitting diode with high brightness and stretchability via elastic-microphase-engineered emitter and dual-embedded electrode. *Light Sci. Appl.* **15**, 182 (2026).
31. Zhuo, Z. et al. Intrinsically stretchable fully π-conjugated polymer film via fluid conjugated molecular external plasticizing for flexible light-emitting diodes. *Nat. Commun.* **15**, 7990 (2024).

32. Chen, W. et al. Elastic-plastic fully π-conjugated polymer with excellent energy dissipation capacity for ultra-deep-blue flexible polymer light-emitting diodes with CIE_y = 0.04. *Adv. Mater.* **36**, 2402708 (2024).
33. Lv, D. et al. Inkjet printing of silver nanowire electrodes for fully stretchable organic light-emitting diodes. *J. Mater. Chem. C.* **14**, 2800–2813 (2026).
34. Lee, W. et al. Hybrid liquid metal cathode enables high-performance intrinsically stretchable OLEDs. *Adv. Mater.* **38**, e18254 (2026).
35. Oh, J. H. et al. Intrinsically stretchable phosphorescent light-emitting materials for stretchable displays. *ACS Appl. Mater. Interfaces.* **15**, 33784–33796 (2023).
36. Gu, J. et al. Intrinsically stretchable organic light-emitting layers by using a high-vinyl polybutadiene elastomer blended with small molecule/polymer hosts and a highly doped TADF guest. *Chem. Eng. J.* **522**, 167506 (2025).
37. Ha, H. et al. Intrinsically stretchable emissive layer for green and red phosphorescent OLEDs: small molecules blended with SEBS elastomer. *Adv. Mater. Technol.* **8**, 2300924 (2023).
38. Zhou, H. et al. Exciplex-enabled high-efficiency, fully stretchable OLEDs. *Nature*. **649**, 604–611 (2026).
39. Liu, W. et al. High-efficiency stretchable light-emitting polymers from thermally activated delayed fluorescence. *Nat. Mater.* **22**, 737–745 (2023).
40. Liu, W. et al. Enabling efficient electron injection in stretchable OLED. *Nat. Mater.* **25**, 472–480 (2026).
41. Wang, G. et al. Approaching-unity PLQY and high stretchability in polymer emitters via molecular spacers. *Nat. Commun*. **17**, 6719 (2026).